Mon. Not. R. Astron. Soc. **391,** 1239–1258 (2008) doi:10.1111/j.1365-2966.2008.13930.x

Dynamics of the solar tachocline – II. The stratified case

P. Garaud[1]⋆ and J.-D. Garaud[2]

[1]*Department of Applied Mathematics and Statistics, Baskin School of Engineering, University of California, Santa Cruz, USA*
[2]*Centre des Matériaux, Mines Paristech/CNRS UMR 7633, Evry, France*

Accepted 2008 September 8. Received 2008 September 8; in original form 2008 June 15

ABSTRACT

We present a detailed numerical study of the Gough & McIntyre model for the solar tachocline. This model explains the uniformity of the rotation profile observed in the bulk of the radiative zone by the presence of a large-scale primordial magnetic field, confined below the tachocline by flows originating from within the convection zone. We attribute the failure of previous numerical attempts at reproducing even qualitatively Gough & McIntyre's idea to the use of inappropriate boundary conditions at the radiative–convective interface. We emphasize the key role of flows downwelling from the convection zone in confining the assumed internal field. We carefully select the range of parameters used in the simulations to guarantee a faithful representation of the hierarchy of expected length-scales. We then present, for the first time, a fully non-linear and self-consistent numerical solution of the Gough & McIntyre model which qualitatively satisfies the following set of observational constraints: (i) the quenching of the large-scale differential rotation below the tachocline – including in the polar regions – as seen by helioseismology (ii) the confinement of the large-scale meridional flows to the uppermost layers of the radiative zone as required by observed light element abundances and suggested by helioseismic sound-speed data.

Key words: MHD – Sun: interior – Sun: magnetic fields – Sun: rotation.

1 INTRODUCTION

The presence of the tachocline, a thin shear layer located at the interface between the radiative and convective regions of the Sun, was established two decades ago (Christensen-Dalsgaard & Schou 1988; Kosovichev 1988; Brown et al. 1989; Dziembowski, Goode & Libbrecht 1989) but its *modus operandi* still remains mysterious.

Anisotropic turbulent stresses associated with rotationally constrained eddies are thought to maintain the differential rotation profile $\Omega_{\rm cz}(\theta, r)$ observed within the convection zone:

$$\Omega_{\rm cz}(\theta, r) \simeq \Omega_{\rm eq}(r)\left[1 - a_2(r)\cos^2\theta - a_4(r)\cos^4\theta\right], \quad (1)$$

where for example at $r = 0.75\,{\rm R}_\odot$, $\Omega_{\rm eq}/2\pi = 463$ nHz, $a_2 = 0.17$ and $a_4 = 0.08$ (Schou et al. 1998; Gough 2007). Spiegel & Zahn (1992, SZ92 hereafter) showed that this differential rotation is expected to subsist below the base of the convection zone (at $r_{\rm cz} = 0.713\,{\rm R}_\odot$), despite the expected reduction in the amplitude of the turbulent stresses. In fact, they showed how the *absence* of turbulent stresses in the tachocline region would *permit* the propagation of the latitudinal shear through radiative diffusion, which is clearly at odds with observations. The observed thickness of the tachocline therefore suggests the presence of efficient and anisotropic angular momentum transporters near the radiative–convective interface.

⋆E-mail: pgaraud@ams.ucsc.edu

It was later argued by Gough & McIntyre (1998) (GM98 hereafter) that only magnetic stresses can explain the suppression of the rotational shear throughout the bulk of the radiative zone and in addition maintain the angular velocity of the interior (observed to be $\Omega_{\rm rz}/2\pi \simeq 430$ nHz) close to that of the surface despite the global spin-down induced by magnetic braking. Indeed, it has long been known that even a very small primordial magnetic field embedded in the radiative zone could in principle impose uniform rotation (Ferraro 1937; Mestel 1953; Mestel & Weiss 1987). Ferraro's isorotation law,

$$\boldsymbol{B}\cdot\nabla\Omega = 0, \quad (2)$$

valid in the limit of negligible dissipation and for steady state, axisymmetric flows, is usually stated as *the angular velocity must be constant on magnetic field lines*. Thus in its simplest form, Ferraro's law predicts the possibility of uniform rotation for the radiative zone provided the magnetic field is entirely confined beneath the radiative–convective interface (Rüdiger & Kitchatinov 1997). On the other hand, any field line directly connected with the convection zone promotes the propagation of the rotational shear into the radiative zone (MacGregor & Charbonneau 1999), inducing what will be referred to from here on as a 'differentially rotating Ferraro state'. Hence, field confinement appears to be the key to the existence of a tachocline.

GM98 were the first to address the question of how the presumed primordial field could indeed be confined within the radiative zone,

and proposed that downward burrowing meridional flows driven by Coriolis forces in the convection zone would interact non-linearly with the underlying magnetic field lines, bending them towards the horizontal in the tachocline region, thus effectively suppressing direct radial Alfvénic transport between the convection zone and the radiative zone. Conveniently, the same meridional flows can also be held responsible for mixing light elements such as Li and Be between the convection zone and their respective nuclear burning regions, reducing He settling (Elliott & Gough 1999) as well as providing weak but sufficient angular momentum transport to adjust the mean rotation rates of the convective and radiative zones continuously throughout the spin-down phase. The seminal boundary-layer analysis of the dynamics of the tachocline presented by GM98 validated the plausibility of this theory, although many of their simplifying scaling assumptions remain to be confirmed through the direct numerical solution of the governing equations.

This paper first briefly reviews existing work and then presents new results on the laminar tachocline dynamics according to GM98. We begin by discussing past attempts at implementing their model numerically in Section 2. In particular, we argue that the failure of previous numerical studies in reproducing field confinement can be explained by the selection of inappropriate boundary conditions. A new numerical algorithm is then presented in Section 3, and used in Section 4 to revisit the idea proposed by GM98 with much more success. We discuss future prospects in Section 5.

2 DISCUSSION OF PREVIOUS NUMERICAL MODELS IN THE LIGHT OF GOUGH & MCINTYRE'S ORIGINAL IDEA

GM98 argue that the radiative interior should be divided into three dynamically distinct zones including (from the base of the convection zone downward) (1) a more or less magnetic-free region in thermal-wind balance, well ventilated by meridional flows originating from the convection zone, which can be thought of as the bulk of the tachocline, (2) a very thin magnetic advection–diffusion layer where the tachocline flows and the underlying field interact non-linearly to confine one another and (3) a magnetically dominated, near-uniformly rotating interior.

The non-linear nature and geometric complexity of the problem precludes analytical solutions, and all existing studies since the original work of GM98 have been numerical (see the review by Garaud 2007). Among these, only two include all the non-linear terms required (i.e. the inertial terms and the Lorentz force in the momentum equation and the induction term in the magnetic induction equation) to represent the magnetohydrodynamics of the tachocline 'correctly': Garaud (2002) – hereafter Paper I – and Brun & Zahn (2006) – hereafter BZ06. Surprisingly, neither has been able to find evidence for the kind of dynamical balance proposed by GM98, and the time is therefore ripe to take a step back and discuss why.

2.1 'Failure' of previous numerical models

Paper I and BZ06 both model magnetohydrodynamic perturbations induced in the solar radiative zone by the differentially rotating convection zone and by an assumed primordial magnetic field. Both papers focus on the issues of field confinement and the suppression of differential rotation below the tachocline.

Paper I presents steady state, axially symmetric solutions of an incompressible and unstratified version of the GM98 model. BZ06 on the other hand use a time-dependent, 3D algorithm based on the ASH code (Glatzmaier 1984; Clune et al. 1999; Miesch et al. 2000; Brun, Miesch & Toomre 2004), and solve the complete set of anelastic MHD equations. Both studies otherwise consider a similar computational domain, namely a spherical shell which spans the region between the base of the convection zone (at $r = r_{\rm out} \simeq r_{\rm cz}$) and an inner sphere (at $r = r_{\rm in}$). The boundary conditions are also essentially similar: the 'outer' boundary, which effectively models the radiative–convective interface, is in both cases assumed to be impermeable and rotating differentially with an angular velocity profile given by equation (1); the magnetic field is matched on to a potential field.

In Paper I, the numerical solutions only show confinement of the magnetic field lines in the equatorial regions for low enough diffusivities, occasionally at mid-latitudes for lower field strength, but never in the polar regions (see fig. 11 of Paper I for example). It is commonly argued that the failure of Paper I to find fully confined magnetic field solutions stems entirely from the simplified nature of the model equations (incompressible, unstratified): indeed, within these assumptions the meridional flows are generated only by Ekman–Hartmann pumping on the boundaries, and their amplitude scales with the diffusivities in a way which always maintains the magnetic Reynolds number below unity. As a result, these flows are unable to confine the magnetic field and the differential rotation imposed at the upper boundary of the domain persists within a large part of the radiative zone.

The 3D, time-dependent solutions of BZ06 naturally depend on the initial magnetic field configuration selected. Various cases with an initial field more or less deeply confined are discussed. Against expectations, BZ06 find that regardless of the initial conditions, the field lines always spread out and eventually overlap with the convection zone, permitting the propagation of the differential rotation into the radiative interior. Interestingly, the transient state of the system – prior to any field line connecting with the convection zone – qualitatively looks in many ways similar to the well-known GM98 picture, although it is clearly not a steady state. The 'tachocline' thus formed slowly narrows with time until field lines spread into the convection zone, at which point a differentially rotating Ferraro state is rapidly established. One is forced to conclude in one of three ways: (1) for unspecified primordial reasons, the initial magnetic field was more deeply embedded in the radiative zone and the currently observed tachocline is merely a transient phase; (2) the tachocline is indeed in a steady state and some of the assumptions made on the way were wrong; (3) the parameter regime studied by BZ06 (where diffusion coefficients are artificially increased by many orders of magnitude to satisfy numerical constraints) does not appropriately reproduce the solar interior dynamics.

One should be uncomfortable in selecting the first option, as it would place very strong and unlikely constraints on the initial field conditions to provide just the right structure for today's tachocline. One could naively tend to favour the third option, but BZ06 a priori took care to select a range of parameters for which all expected boundary layer thicknesses are small enough and in the same hierarchical order as those of the model proposed by GM98. The plot thickens while we are left with the uneasy task of reconsidering the key features of either the numerical models or of the GM98 model (both, perhaps).

2.2 The source of the problem

At this point it is worth discussing one of the more delicate aspects of the GM98 model, namely the exact mechanism by which these pivotal meridional flows are thought to be generated. This point has been a source of confusion and debate, but is clearly crucial to a

better understanding of the tachocline dynamics. In the original work of GM98, the principal clue to the nature of the flows can be found in the sentence: '*Turbulent stresses in the convection zone induce (through Coriolis effects) a meridional circulation, causing the gas from the convection zone to burrow downwards . . .*'. The flows considered by GM98 do not originate from within the tachocline and can therefore not be appropriately modelled by a numerical scheme in which the radiative–convective interface is assumed to be impermeable (as it is done in Paper I and BZ06). While this conclusion seems obvious in hindsight, the physics of the problem are actually rather subtle and deserve clarification. In what follows, we discuss the issue in more detail and present a unified view of the results of previous works on the subject.

Spiegel & Zahn were the first to study the dynamics of the newly discovered tachocline (SZ92). They considered a non-magnetic radiative zone only, and imposed a latitudinally varying rotation profile at the radiative–convective interface. They performed two distinct calculations. The first looked at the time-dependent evolution of the angular velocity profile in the radiative zone under such forcing, assuming isotropic viscous stresses. The second sought steady state 'tachocline' solutions assuming anisotropic turbulent stresses. Since the latter did not specifically address the question of the meridional flows, we focus here on the results of the time-dependent calculation, which can be interpreted in the following way. The differential rotation imposed by the convection zone to the top of the radiative zone inevitably induces some degree of shear along the rotation axis if the radiative zone is originally in a state of uniform rotation. This generates a thermal gradient in the latitudinal direction by way of the thermal-wind equation (see GM98, equation 1 for example). Meridional flows are then required to balance this thermal gradient when the system is in thermal equilibrium. These flows burrow into the radiative zone, advecting angular momentum thereby helping the propagation of the shear further down. The results of SZ92 imply that the system continues evolving in this fashion until the radiative zone has achieved complete thermal and dynamical equilibrium.

The characteristic amplitude of the time-dependent flows associated with this thermodynamical relaxation process is, by way of the assumptions listed above, only dependent on the (evolving) local differential rotation, stratification and thermal conductivity. Their turnover time-scale is calculated to be of the order of the local Eddington–Sweet time-scale, which is short in the initial relaxation stages and steadily increases as the system evolves. Crucially, this result was derived independently of any boundary condition on the meridional flows. It is therefore correct to think of the induced transient flows as being driven by baroclinic stresses from *within* the tachocline rather than downwelling from the convection zone. In fact, they exist *even if* the radiative–convective interface is assumed to be impermeable. This fact is probably at the origin of the impermeable boundary conditions selected by Paper I and by BZ06, in spite the obvious contradiction with GM98's intent.

However, it is vital to remember that this transient phase and its associated flows both end once the system achieves thermal and dynamical equilibrium. The only flows remaining in the final steady state are driven, within tiny boundary layers, by the thermo(magneto)viscous stresses required to match the bulk equilibrium solutions to the applied boundary conditions. Thus, as expected from any elliptic problem, the nature of the boundary conditions selected entirely controls the steady state solutions. This is clearly illustrated by the work of Garaud & Brummell (2008) (GB08 hereafter), which complements that of SZ92 by calculating the spatial properties as well as characteristic amplitudes of *steady state* meridional flows in the radiative zone, as induced by various kinds of forcing applied at the radiative–convective interface.

GB08 showed that in the non-magnetic case, the induced steady state flows can always be viewed – at least in the linear sense, and for solar parameters – as the sum of two 'modes': a viscously dominated 'Ekman mode', which very rapidly decays away from the interface (on an Ekman length-scale), and a 'thermoviscous mode' which can essentially span the entire radiative zone when not hindered by a magnetic field. Since the Ekman mode a priori decays too rapidly to have any effect on the tachocline dynamics, the flows discussed by GM98, which are thought to ventilate the bulk of the tachocline, should be identified with the thermoviscous mode. This view is perfectly consistent with GM98's analysis, since the thermoviscous mode is in thermal-wind balance (GB08).

The respective amplitudes with which the Ekman and thermoviscous modes are driven depend on the nature, amplitude and spatial structure of the forcing. GB08 showed that when the interface is impermeable, as assumed in Paper I and by BZ06, then the amplitude of the thermoviscous mode is negligible for microscopic solar values of the diffusivities. As a result, the magnetic Reynolds number of these tachocline flows is much smaller than unity, which straightforwardly explains why field confinement eluded these two previous studies.

When flows are pumped directly through the interface by stresses within the convection zone (i.e. the radial component of the flows is non-zero at the radiative–convective interface), GB08 find that the amplitude of the thermoviscous mode can be much higher, in which case the tachocline flows may be expected to confine the field in a scenario qualitatively similar to the one proposed by GM98. The quantitative detailed analysis must be done numerically; this is the purpose of the present study.

3 THE NUMERICAL MODEL

We now revisit the idea proposed by GM98 in the light of the previous discussion. A new numerical algorithm has been constructed specifically for this purpose. We first present, for the sake of completeness, a derivation of our model equations in Section 3.1. Since our computational domain is limited to a spherical shell within the radiative zone, we then present and discuss in detail all the boundary conditions applied in Section 3.2. The relevant non-dimensional parameters and expected boundary layers of the problem are discussed in Section 3.3. The numerical method, as well as other numerical constraints, are finally outlined in Section 3.4.

3.1 The governing equations

The standard solar model (SSM hereafter) provides an accurate representation of the thermal structure and composition of the interior of a hypothetical spherically symmetric, non-rotating, non-magnetic Sun. The excellent match between the SSM and helioseismic observations confirms that the likely internal dynamics of the Sun only induce weak deviations in the background state thermodynamical quantities. The large-scale magnetohydrodynamics of the solar interior, thought to be responsible for the maintenance of the peculiar observed rotation profile, can therefore be thought of as perturbations upon the SSM.

The quasi-steady SSM equations (which are valid on time-scales much shorter than the nuclear burning time-scale) reduce to the following set of four equations within the solar radiative zone (but

outside of the nuclear burning core):

$$
\begin{aligned}
&-\nabla\overline{p} = \overline{\rho}\nabla\overline{\Phi},\\
&\nabla\cdot(\overline{k}\nabla\overline{T}) = 0,\\
&\overline{p} = \overline{p}(\overline{\rho},\overline{T}),\\
&\nabla^2\overline{\Phi} = 4\pi G\overline{\rho}.
\end{aligned}
\tag{3}
$$

These equations describe hydrostatic equilibrium, thermal equilibrium, the equation of state and finally the Poisson equation for the gravitational potential, respectively. Here, ρ, T and p are the standard thermodynamical variables, k is the thermal conductivity (which typically depends on T and ρ), G is the gravitational constant and Φ is the gravitational potential. The equation of state itself is well approximated by that of a perfect gas in this region of the Sun. The solution to the set of equations (3) for the present-day Sun can be inferred from model S of Christensen-Dalsgaard et al. (1996) for example (see Appendix A).

We then consider perturbations on this background equilibrium caused by meridional and azimuthal flows, as well as magnetic fields. For simplicity, we restrict our study to axisymmetric systems. Moreover, since the observed internal rotation profile of the Sun has remained approximately constant over the past decade, we boldly postulate that the Sun is in fact in a state of quasi-steady dynamical and thermal balance. The general set of equations governing the axisymmetric, quasi-steady perturbations, are then

$$
\begin{aligned}
&\rho\boldsymbol{u}\cdot\nabla\boldsymbol{u} = -\nabla p - \rho\nabla\Phi + \boldsymbol{j}\times\boldsymbol{B} + \nabla\cdot\Pi,\\
&\nabla\cdot(\rho\boldsymbol{u}) = 0,\\
&\rho T\boldsymbol{u}\cdot\nabla s = \nabla\cdot(k\nabla T),\\
&p = p(\rho,T),\\
&\nabla^2\Phi = 4\pi G\rho,\\
&\nabla\times(\boldsymbol{u}\times\boldsymbol{B}) = \nabla\times(\eta\nabla\times\boldsymbol{B}),\\
&\nabla\cdot\boldsymbol{B} = 0,
\end{aligned}
\tag{4}
$$

where $\boldsymbol{u}$ represents the axisymmetric flow velocity, $\boldsymbol{B}$ the magnetic field and $\boldsymbol{j} = \nabla\times\boldsymbol{B}/4\pi$ is the electric current, Π is the viscous stress tensor, s is the specific entropy and η is the magnetic diffusivity. These equations, respectively, characterize the conservation of momentum, mass and thermal energy, the equation of state and the Poisson equation, conservation of magnetic flux and finally, the solenoidal condition.

Thermodynamical perturbations are from here on denoted with tildes, as for example in $p = \overline{p} + \tilde{p}$. The system of equations (4) can be linearized in the thermodynamical quantities around the background state equations (3) to yield

$$
\begin{aligned}
&\overline{\rho}\boldsymbol{u}\cdot\nabla\boldsymbol{u} = -\nabla\tilde{p} - \overline{\rho}\nabla\tilde{\Phi} - \tilde{\rho}\nabla\overline{\Phi} + \boldsymbol{j}\times\boldsymbol{B} + \nabla\cdot\Pi,\\
&\nabla\cdot(\overline{\rho}\boldsymbol{u}) = 0,\\
&\overline{\rho}\overline{T}\boldsymbol{u}\cdot\nabla\overline{s} = \nabla\cdot(\overline{k}\nabla\tilde{T}),\\
&\frac{\tilde{p}}{\overline{p}} = \frac{\tilde{\rho}}{\overline{\rho}} + \frac{\tilde{T}}{\overline{T}},\\
&\nabla^2\tilde{\Phi} = 4\pi G\tilde{\rho},\\
&\nabla\times(\boldsymbol{u}\times\boldsymbol{B}) = \nabla\times(\overline{\eta}\nabla\times\boldsymbol{B}),\\
&\nabla\cdot\boldsymbol{B} = 0,
\end{aligned}
\tag{5}
$$

where we approximated the equation of state with that of a perfect gas, and neglected perturbations to the chemical composition. Note that the latter approximation was chosen for the sake of simplicity: Wood & McIntyre (2007) showed that the effects of compositional gradients (notably helium) could play an important role in the tachocline dynamics. The background magnetic diffusivity $\overline{\eta}$, kinematic viscosity $\overline{\nu}$ and thermal conductivity $\overline{k}$ are calculated from model S using the expressions provided by Gough (2007) (see Appendix A).

Note that the non-linearities in the quantities relating to the magnetohydrodynamics of the interior (flow velocities and magnetic field) have not yet been tampered with.[1] The next step is to use a spherical coordinate system (r,θ,ϕ) and move to a rotating frame of reference, by considering that $\boldsymbol{u} = \overline{\boldsymbol{u}} + \tilde{\boldsymbol{u}}$, with $\overline{\boldsymbol{u}} = r\sin\theta\overline{\Omega}\hat{\boldsymbol{e}}_\phi$ and $\tilde{\boldsymbol{u}} = (\tilde{u}_r,\tilde{u}_\theta,\tilde{u}_\phi)$. The value of $\overline{\Omega}$ adopted is uniquely defined by requiring that the total angular momentum of the convection zone be null in the rotating frame (Gilman, Morrow & Deluca 1989): if $\Omega_{\rm cz}(\theta,r)$ is assumed to be independent of radius, and given by equation (1), then

$$
\overline{\Omega} = \Omega_{\rm eq}\left(1 - \frac{a_2}{5} - \frac{3a_4}{35}\right). \tag{6}
$$

The equation for the conservation of momentum then becomes

$$
\begin{aligned}
&\overline{\rho}\tilde{\boldsymbol{u}}\cdot\nabla\tilde{\boldsymbol{u}} + 2\overline{\rho}\overline{\boldsymbol{\Omega}}\times\tilde{\boldsymbol{u}} + \overline{\rho}\overline{\boldsymbol{\Omega}}\times\overline{\boldsymbol{\Omega}}\times\boldsymbol{r}\\
&\quad = -\nabla\tilde{p} - \overline{\rho}\nabla\tilde{\Phi} - \tilde{\rho}\nabla\overline{\Phi} + \boldsymbol{j}\times\boldsymbol{B} + \nabla\cdot\Pi,
\end{aligned}
\tag{7}
$$

while the assumption of axial symmetry implies that the equations for the conservations of mass, thermal energy and magnetic flux are merely changed by replacing $\boldsymbol{u}$ with $\tilde{\boldsymbol{u}}$.

It is well known that the baroclinic deformation of the background state caused by the centrifugal force drives meridional flows, albeit very slow ones since the Sun is a slow rotator (Eddington 1925; Sweet 1950). Since the global turnover timescale of this Eddington–Sweet circulation is calculated to be orders of magnitude longer than the age of the Sun, it cannot play any role in the angular momentum or chemical mixing processes. In a steady state calculation, however, these flows play an artificially inflated role and it is important to suppress them. This can be done by using the following momentum conservation equation instead (SZ92):

$$
\overline{\rho}\tilde{\boldsymbol{u}}\cdot\nabla\tilde{\boldsymbol{u}} + 2\overline{\rho}\overline{\boldsymbol{\Omega}}\times\tilde{\boldsymbol{u}} = -\nabla\tilde{p} - \tilde{\rho}\nabla\overline{\Phi} + \boldsymbol{j}\times\boldsymbol{B} + \nabla\cdot\Pi, \tag{8}
$$

where Cowling's approximation was also used to justify neglecting the perturbation of the gravitational potential related to density and temperature perturbations caused by the remaining Coriolis and Lorentz forces.

Finally, we assume that the meridional flow velocities remain small (SZ92; GM98): we neglect quadratic terms in $\tilde{u}_r$ and $\tilde{u}_\theta$, but retain non-linearities in $\tilde{u}_\phi$ to allow for significant differential rotation.

To summarize, the model equations we consider are

$$
\begin{aligned}
&\overline{\rho}\tilde{\boldsymbol{u}}\cdot\nabla\tilde{\boldsymbol{u}} + 2\overline{\rho}\overline{\boldsymbol{\Omega}}\times\tilde{\boldsymbol{u}} = -\nabla\tilde{p} - \tilde{\rho}\nabla\overline{\Phi} + \boldsymbol{j}\times\boldsymbol{B} + \nabla\cdot\Pi,\\
&\nabla\cdot(\overline{\rho}\tilde{\boldsymbol{u}}) = 0,\\
&\overline{\rho}\overline{T}\tilde{\boldsymbol{u}}\cdot\nabla\overline{s} = \nabla\cdot(\overline{k}\nabla\tilde{T}),\\
&\frac{\tilde{p}}{\overline{p}} = \frac{\tilde{\rho}}{\overline{\rho}} + \frac{\tilde{T}}{\overline{T}},\\
&\nabla\times(\tilde{\boldsymbol{u}}\times\boldsymbol{B}) = \nabla\times(\overline{\eta}\nabla\times\boldsymbol{B}),\\
&\nabla\cdot\boldsymbol{B} = 0,
\end{aligned}
\tag{9}
$$

[1] Also note that in principle, the thermal energy equation should contain an additional term, namely $\tilde{k}\nabla\overline{T}$. This term is included in the numerical algorithm for the sake of completeness, but in practise has little influence on the result (at least in the case of the solar radiative zone). It will not be discussed in this paper for the sake of simplicity.

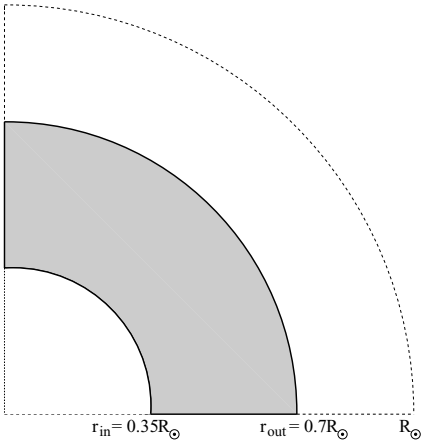

Figure 1. The computational domain is limited to the spherical shell shown here in grey.

where the quantities solved for are the three components of $\tilde{\boldsymbol{u}}$ (as defined above), the three components of $\boldsymbol{B} = (B_r, B_\theta, B_\phi)$, and the three thermodynamical variables $\tilde{p}$, $\tilde{\rho}$ and $\tilde{T}$, and where quadratic terms in $\tilde{u}_r^2$, $\tilde{u}_\theta^2$ and $\tilde{u}_r\tilde{u}_\theta$ are neglected (see Appendix B for the full set of equations expanded in a spherical coordinate system).

This set of equations is equivalent to the one used by GM98 before they apply their boundary-layer analysis. It also reduces to the one used by SZ92 in the non-magnetic case, provided the following further approximations are applied: the Boussinesq approximation, assuming that $\tilde{\Omega} \ll \overline{\Omega}$ and that $\tilde{u}_\theta \gg \tilde{u}_r$. Finally, it is a steady state and axisymmetric version of the equations used by BZ06.

For comparison, note that Rüdiger & Kitchatinov (1997), MacGregor & Charbonneau (1999) and Kitchatinov & Rüdiger (2006) neglect meridional flows entirely in their calculations of the structure of the radiative interior.[2] Sule, Rüdiger & Arlt (2005) include meridional flows but assume that the poloidal field is fixed, so that the interaction between the field and the flows through the Lorentz force in their paper is fundamentally linear (and therefore inappropriate).

3.2 Domain boundaries and boundary conditions

3.2.1 Computational domain

The geometry of the computational domain is shown in Fig. 1. The upper boundary is selected to be slightly below the base of the convection zone, at $r_{\rm out} = 0.7\,\mathrm{R}_\odot$. The lower boundary is at $r_{\rm in} = 0.35\,\mathrm{R}_\odot$ as in BZ06. The inner core (for $r < r_{\rm in}$) can be viewed as a solid metallic sphere, within which a permanent magnetic dipole is maintained. The selection of the position of the lower boundary was found to have little influence on the tachocline dynamics for low enough values of the diffusivities.

3.2.2 Model boundary conditions

The selection of adequate boundary conditions for this model is a very delicate task. Given the elliptic and non-linear nature of the system considered, the existence of solutions is not guaranteed, and solutions (when they exist) are entirely controlled by the boundary conditions applied.

Our aim is to propose a set of boundary conditions at the upper boundary of the computational domain which reproduces most faithfully the influence of the convection zone on the radiative zone, while those near the lower boundary are selected in such a way as to impose the required dipolar field, but otherwise be as inconspicuous as possible.

The set of coupled partial differential equations described in (9) and expanded in Appendix B represents a 12th-order system, and therefore requires 12 independent boundary conditions.

Bottom boundary conditions. The bottom boundary of the computational domain is located at $r_{\rm in}$, and should be thought of as the interface between the modelled fluid and an electrically and thermally conducting solid sphere (hereafter 'the core'). Impermeability implies

$$\tilde{u}_r = 0 \quad \text{at } r = r_{\rm in}. \tag{10}$$

We generally impose no-slip boundary conditions at $r_{\rm in}$ (except when specifically mentioned), so that $\tilde{u}_\theta = 0$ and $\tilde{u}_\phi = r_{\rm in}\sin\theta\tilde{\Omega}_{\rm in}$, where $\tilde{\Omega}_{\rm in}$ is the constant angular velocity of the core in the rotating frame. The value of $\tilde{\Omega}_{\rm in}$ is selected in such a way as to guarantee that the total torque applied to the core be zero:

$$\int_{-\pi/2}^{\pi/2}\left(\overline{\rho v} r_{\rm in}^2\sin^2\theta\frac{\partial\tilde{\Omega}}{\partial r} + r_{\rm in}\sin\theta\frac{B_r B_\phi}{4\pi}\right)\sin\theta\,\mathrm{d}\theta = 0. \tag{11}$$

Assuming that the core is a homogeneous thermally conducting solid implies that the temperature fluctuations within satisfy Laplace's equation

$$\nabla^2\tilde{T}^{\rm in} = 0. \tag{12}$$

The regular solution can be expanded upon standard eigenfunctions, namely

$$\tilde{T}^{\rm in}(r,\theta) = \sum_{n=0}^{\infty} a_n^{\rm in} P_n(\cos\theta)\, r^n, \tag{13}$$

where P_n is the nth-order Legendre polynomial, and the set $\{a_n^{\rm in}\}$ are integration constants. Requiring the simultaneous continuity of $\tilde{T}$ and its derivative at $r = r_{\rm in}$ while satisfying equation (13) constrains the $\{a_n^{\rm in}\}$ and yields a unique relationship between $\tilde{T}$ and $\partial\tilde{T}/\partial r$, which is used as a boundary condition on temperature.

Two boundary conditions for the magnetic field are required. They are obtained in a similar fashion to that of the temperature fluctuations, by assuming that the core is a homogeneous electrically conducting solid with the same conductivity as the fluid nearby. In that case the magnetic field within satisfies

$$\nabla^2\boldsymbol{B}^{\rm in} = 0, \tag{14}$$

which, by axial symmetry, is equivalent to

$$(\nabla^2\boldsymbol{B}^{\rm in})_\phi = 0 \text{ and } (\nabla\times\boldsymbol{B}^{\rm in})_\phi = 0. \tag{15}$$

Defining a flux function χ as

$$\boldsymbol{B}_{\rm p}^{\rm in} = \nabla\times\left(\chi^{\rm in}\hat{\boldsymbol{e}}_\phi\right) \tag{16}$$

implies that both $B_\phi^{\rm in}$ and $\chi^{\rm in}$ satisfy the same equation, namely

$$\nabla^2 B_\phi^{\rm in} - \frac{B_\phi^{\rm in}}{r^2\sin^2\theta} = 0, \quad \text{similarly for} \chi^{\rm in}. \tag{17}$$

The regular solution for $B_\phi^{\rm in}$ can be expanded as

$$B_\phi^{\rm in}(r,\theta) = \sum_{n=1}^{\infty} b_n^{\rm in}\frac{\partial}{\partial\theta}\left[P_n(\cos\theta)\right] r^n, \tag{18}$$

[2] Although in work of Kitchatinov & Rüdiger (2006), the effect of the flows is assumed to influence the boundary conditions applied to the magnetic field.

where as before the $\{b_n^{\rm in}\}$ are integration constants. Requiring the simultaneous continuity of B_ϕ and its derivative at $r = r_{\rm in}$ while satisfying equation (18) yields a unique relationship between B_ϕ and $\partial B_\phi/\partial r$, which is used as one of the two required boundary conditions on the magnetic field.

A point dipole located at $r = 0$ is required to maintain the primordial magnetic field in this steady state study. Note that this implicitly assumes that the dynamics of the tachocline occur on time-scales much shorter than the global magnetic diffusion time (which is a reasonable assumption since the global magnetic diffusion time-scale is of the order of the age of the Sun). To match $\boldsymbol{B}_{\rm p}^{\rm in}$ to a point dipole of amplitude B_0 at $r = r_{\rm in}$ and $\theta = 0$ (on the polar axis), we require that

$$\chi^{\rm in} = B_0 \frac{r_{\rm in}^3}{2} \frac{\sin\theta}{r^2} + \sum_{n=1}^{\infty} c_n^{\rm in} \frac{\partial}{\partial\theta} [P_n(\cos\theta)]\, r^n. \tag{19}$$

Requiring the simultaneous continuity of B_r and B_θ at $r = r_{\rm in}$ provides a relationship between these two quantities, which is used as the second of the two required boundary conditions on the magnetic field.

Top boundary conditions. The choice of boundary conditions near the top boundary should model the effects of the convective zone dynamics on the radiative–convective interface.

Requiring the continuity of the angular velocity profile across the interface is a natural choice for the boundary condition on $\tilde{u}_\phi$, although one must bear in mind that it is intrinsically equivalent to assuming that the interface is a no-slip boundary. For consistency, a similar condition should then also be imposed on the other component of the meridional flow parallel to the boundary, $\tilde{u}_\theta$. Hence we select

$$\begin{aligned} \tilde{u}_\theta(r_{\rm out}, \theta) &= u_\theta^{\rm out}(\theta), \\ \tilde{u}_\phi(r_{\rm out}, \theta) &= r_{\rm out} \sin\theta [\Omega_{\rm cz}(\theta) - \overline{\Omega}], \end{aligned} \tag{20}$$

where $u_\theta^{\rm out}(\theta)$ could be any desired latitudinal velocity profile, and $\Omega_{\rm cz}$ is given by equation (1).

Boundary conditions are also needed on the vertical velocity $\tilde{u}_r$. In previous models of the radiative zone (Paper I; BZ06), the radiative–convective interface was assumed to be impermeable. However, this boundary condition is inadequate as a model of a (permeable) fluid interface (see Section 2.2). Instead, we consider the more general distribution

$$\tilde{u}_r(r_{\rm out}, \theta) = u_r^{\rm out}(\theta), \tag{21}$$

where the profile selected for $u_r^{\rm out}(\theta)$ is discussed in more detail in Section 4.2.1.

The temperature boundary condition near the upper boundary is selected to model a very efficiently conducting fluid, by requiring that

$$\nabla^2 \tilde{T}^{\rm out} = 0 \tag{22}$$

outward of the computational domain. Matching $\tilde{T}$ to $\tilde{T}^{\rm out}$ provides a unique relationship between $\tilde{T}$ and $\partial\tilde{T}/\partial r$ at the outer boundary. Note that this boundary condition differs from the one used by BZ06 ($\partial\tilde{S}/\partial r = 0$) and from the one used by SZ92 ($\partial\tilde{\Omega}/\partial r = 0$, which follows through from combining the assumption of geostrophy with the continuity of the temperature across the interface, and observations of the rotation profile in the convection zone).

The boundary conditions for the magnetic field are obtained by assuming that the convection zone is an infinite diffusive medium (with the same diffusivity as that of the fluid at $r = r_{\rm out}$) so that $\nabla^2\, \boldsymbol{B}^{\rm out} = 0$ outward of $r_{\rm out}$) and selecting the solution which decays as $r \to \infty$:

$$\begin{aligned} B_\phi^{\rm out}(r,\theta) &= \sum_{n=1}^{\infty} b_n^{\rm out} \frac{\partial}{\partial\theta} [P_n(\cos\theta)]\, r^{-(n+1)}, \\ \chi^{\rm out}(r,\theta) &= \sum_{n=1}^{\infty} c_n^{\rm out} \frac{\partial}{\partial\theta} [P_n(\cos\theta)]\, r^{-(n+1)}. \end{aligned} \tag{23}$$

Matching these solutions at $r = r_{\rm out}$ with the solution for $\boldsymbol{B}$ within the domain provides relationships between B_ϕ and its derivative, and between B_r and B_θ, respectively.

3.3 Non-dimensional parameters and the nature of boundary layers

3.3.1 Enhanced diffusivities

The typical solutions of the set of equations and boundary conditions described in Sections 3.1 and 3.2 are known to contain thin boundary layers and internal layers of various kinds, typically scaling as some (positive) power of the diffusivities. The limited achievable numerical resolution of the algorithm used implies that the set of equations (9) cannot be solved for solar values of these quantities. To address the problem we multiply the diffusivities $\overline{\nu}(r)$, $\overline{\eta}(r)$ and

$$\overline{\kappa}(r) = \frac{\overline{k}}{\overline{\rho} c_{\rm p}} \tag{24}$$

by the enhancement factors f_ν, f_η and f_κ, respectively. When these factors are all selected equal to each other the Prandtl and magnetic Prandlt numbers ($Pr = \overline{\nu}/\overline{\kappa}$ and $Pr_{\rm m} = \overline{\nu}/\overline{\eta}$, respectively) are solar everywhere. Note that we specifically do not view the numerical model diffusivities as 'turbulent diffusivities'. We strive instead to derive characteristic scalings of the solutions with each of the f factors, and understand the asymptotic behaviour of the solutions as they are simultaneously reduced towards unity.

3.3.2 Non-dimensional parameters

A better understanding of the scaling behaviour of the numerical solutions as f_ν, f_η and f_κ are varied can be achieved by working with non-dimensional parameters. In what follows, we scale all distances with the solar radius $\mathrm{R}_\odot$, and all velocities with $\mathrm{R}_\odot\Omega_{\rm eq}$ (see Appendix C for details). The magnetic field strength is scaled by B_0, which is the amplitude of the imposed field on the inner boundary on the polar axis (see equation 19). Within this framework, the following non-dimensional numbers naturally emerge:

$$\begin{aligned} E_\nu &= \frac{f_\nu \overline{\nu}}{\mathrm{R}_\odot^2 \Omega_{\rm eq}} = f_\nu E_\nu^\odot, \\ E_\eta &= \frac{f_\eta \overline{\eta}}{\mathrm{R}_\odot^2 \Omega_{\rm eq}} = f_\eta E_\eta^\odot, \\ E_\kappa &= \frac{f_\kappa \overline{\kappa}}{\mathrm{R}_\odot^2 \Omega_{\rm eq}} = f_\kappa E_\kappa^\odot, \\ Pr &= \frac{E_\nu}{E_\kappa} = \frac{f_\nu}{f_\kappa} Pr^\odot, \\ H &= \sqrt{\frac{\Lambda}{E_\nu E_\eta}} = \frac{H^\odot}{\sqrt{f_\nu f_\eta}} \quad \text{where } \Lambda = \frac{B^2}{4\pi\rho_0 \mathrm{R}_\odot^2 \Omega_{\rm eq}^2}, \\ Bu &= \left(\frac{N D_\rho}{\mathrm{R}_\odot \Omega_{\rm eq}} \right)^2 = Bu^\odot, \end{aligned} \tag{25}$$

where D_ρ is the local density scaleheight ($D_\rho = 8.6 \times 10^9$ cm in the tachocline region) and N is the buoyancy frequency

($N = 8 \times 10^{-4}\,\mathrm{s}^{-1}$ in the tachocline region). All of the numbers defined above actually vary with position within the solar interior. The first three are Ekman numbers, defined as the ratios of the rotation time-scale to the respective diffusion time-scales. The solar Ekman numbers calculated using the microscopic diffusivities at the base of the convection zone are $E_\nu^\odot \simeq 2 \times 10^{-15}$, $E_\eta^\odot = 3 \times 10^{-14}$ and $E_\kappa^\odot = 10^{-9}$, respectively, all well below unity. The fourth is the Prandtl number, equal to 2×10^{-6} near the base of the convection zone in the Sun. The Hartmann number H depends naturally on the magnetic field strength B selected. For $B = 1$ G, $H^\odot = 2 \times 10^8$ at the base of the convection zone, and H scales as the magnetic field strength. The Burger number Bu is of the order of 10^3.

3.3.3 *Expected boundary layers and desirable parameter range*

To run simulations in a parameter regime that is at least in the same asymptotic limit as the Sun, one should bear in mind the following constraints. To be in the non-diffusive regime, one must ensure that all three Ekman numbers in the simulations are well below unity. The f parameters selected for the numerical calculations should therefore remain below $(E_\nu^\odot)^{-1}$, $(E_\eta^\odot)^{-1}$ and $(E_\kappa^\odot)^{-1}$, respectively, and also ensure that the hierarchy $E_\nu \ll E_\eta \ll E_\kappa$ is respected.

In the non-magnetic case, GB08 showed that the characteristic length-scales of the dynamics of the radiative zone (for solar parameter values) can be summarized as $l_1 \sim \mathrm{R}\odot$ (i.e. the entire interior), $l_2 \sim D_\rho/(\sqrt{Pr\mathrm{Bu}}) \sim Pr^{-1/2}(\Omega_{\mathrm{eq}}/N)\,\mathrm{R}_\odot$ (i.e. $l_2 \sim 3\sqrt{f_\kappa/f_\nu}\,\mathrm{R}_\odot$) and $l_3 \sim E_\nu^{1/2}\,\mathrm{R}_\odot$. Hence, to retain the same ordering of length-scales as in the Sun ($l_2 > l_1 \gg l_3$), the factor $\sqrt{f_\kappa/f_\nu}$ must not drop below 1/3, placing very strong constraints on the Prandtl number used in the simulations (i.e. Pr should not exceed $\sim 10 Pr_\odot$).

The typical magnetic boundary layers are reviewed by Acheson & Hide (1973). In the case of a magnetic field parallel to the boundary considered, the nature of the boundary layer depends on the respective sizes of E_ν and H: if $E_\nu > H^{-1}$ then the boundary layer thickness is of the order of $H^{1/2}\,\mathrm{R}_\odot$, while if $E_\nu < H^{-1}$ then the boundary layer thickness scales as $E_\nu^{1/2}\,\mathrm{R}_\odot$ (i.e. the boundary layer is actually of Ekman type). We conclude that for realistic field strengths, the boundary layers in the horizontal field case (e.g. near the equator) will always be of Ekman type. When the magnetic field is oblique, the situation changes: the Ekman regime is recovered when $E_\nu \ll H^{-2}$, while the boundary layer has a magnetic nature when $E_\nu \gg H^{-2}$, in which case its thickness is of the order of $H^{-1}\,\mathrm{R}_\odot$. We therefore conclude that unless the magnetic field strength (in the tachocline) has amplitudes lower than 0.1 G, one may actually expect a Hartmann layer near the radiative–convective interface.

To guarantee that $E_\nu H^2 \gg 1$ in the simulations we need $f_\eta \ll E_\nu^\odot (H^\odot)^2 \sim 10^2$ if the magnetic field is indeed of the order of 1 G as suggested by GM98. This is clearly not an achievable goal, so we must inflate the magnetic field strength artificially to be of the order of 1 T near the outer boundary; in that case the constraint on f_η is much less stringent, with $f_\eta \leq 10^{10}$.

Finally, if we rely on flows downwelling from the convection zone to confine the magnetic field, then the amplitude of the flows assumed at the radiative–convective interface must be large enough for their magnetic Reynolds number R_m to be larger than unity. Since R_m is very loosely defined as

$$R_\mathrm{m} = \frac{|u_r|\Delta}{f_\eta \overline{\eta}}, \tag{26}$$

where $|u_r|$ is the typical amplitude of the radial flows and $\Delta \sim 0.03\,\mathrm{R}_\odot$ is the observed thickness of the tachocline (both in CGS units), then equation (26) implies that we need a priori flows with amplitude of the order of $f_\eta \overline{\eta}/\Delta \sim 2000(f_\eta/10^{10})$ cm s^{-1} to have a magnetic Reynolds number of the order of 1. For values of $f_\eta \sim 10^{10}$ (typically achieved in the simulations), this naturally requires unphysically large flow amplitudes. The consequences of this choice are discussed in Sections 4.3 and 5.

3.4 Numerical method

3.4.1 *Method and tests*

The numerical method selected for the solution of this elliptic system is based on the expansion of the governing equations and boundary conditions upon a truncated set of orthogonal functions spanning the θ direction (Chebishev polynomials to be precise), followed by the solution of the associated set of ordinary differential equations (ODEs) in the r-direction using a second-order Newton–Raphson–Kantorovich (NRK) relaxation algorithm. The numerical algorithm is globally similar to the one used by Garaud (2001) and in Paper I, and is summarized in Appendix C. The high latitudinal resolution required to capture the detailed structure of the interior dynamics demands a high-order expansion in θ. This in turn requires a sophisticated parallelized version of NRK. An outline of RELAX – the parallel NRK algorithm freely available upon request to P. Garaud – is given in Appendix D (see also Garaud & Garaud 2007).

The complexity of the full set of equations (9) precludes the derivation of analytical solutions in the general case, and hence direct tests of the full numerical algorithm. However, we have extensively and successfully tested the code through direct comparisons of the numerical solutions with analytical solutions of selected *subsets* of the system: Paper I tested the unstratified magnetic version of the code, while GB08 tested the stratified non-magnetic version of the code.

3.4.2 *Note on the convergence of the solutions*

In the NRK/RELAX algorithm, a guess is required for the solution of the ODE system, and refined by successive iterations until the desired accuracy is reached. The convergence of the algorithm is guaranteed and immediate for linear systems regardless of the initial guess, but requires more accurate initial guesses for increasingly dominant non-linearities. As a result, solutions are found in practice, first for high values of the diffusivities (i.e. high f) and with a low number of latitudinal modes, and then progressively followed into the non-linear regime by lowering f and increasing the number of modes.

Convergence of the solutions usually becomes painfully difficult as f is lowered below a certain threshold. The causes of the problem can be varied: in some cases, the non-linearities begin to dominate the solution and bifurcations may occur where multiple steady states emerge and reduce the basin of attraction of the solution followed; in others, the spatial structure of the solution becomes finer and finer, requiring more latitudinal modes and more radial meshpoints to be fully resolved.

The only way to address the first problem is to follow the solution carefully, and reduce f only by a very small fraction between each run. This has the disadvantage of being a frustratingly slow process, with little to be gained in practice. As a matter of fact, the likely change of stability of the solution tracked and the emergence of multiple steady solutions (suggested by the change in convergence properties) is an interesting dynamical information in itself (see Section 3.4.3).

To address the second problem typically requires increasing the number of modes and meshpoints, which leads to a very rapid increase in computational costs. None the less, some acceptable trade-offs are found with typical simulations using a few thousand meshpoints (mostly concentrated in the boundary layers) and about 60–100 latitudinal modes. These require no more than a few hours per iteration on about 2^7–2^8 processors (see Appendix D).

3.4.3 Discussion of the selection of the algorithm

At this point it may be worth discussing an oft-raised question about the selection of this specific numerical method of solution, as an alternative to the time-dependent ASH code used by BZ06. Both methods, when taken individually, are equally useful tools for studying the problem, each with their own advantages and limitations.

For example, the algorithm of BZ06 studies the general properties of the radiative zone under the forcing considered, and in addition provides information on the stability of the system, naturally taking into account transport by smaller scale 3D flows when necessary. However, the very lengthy integration time required implies that only very few different parameter values can realistically be explored. Moreover, the time-dependent nature of the algorithm makes it more difficult to identify quasi-steady states (in particular when the typical time-scales in the numerical model are far less obviously separated than in the Sun).

By contrast, the simplified axisymmetric and steady state nature of the equations solved in Paper I and here implies that each solution can be found in at most a day of real-time computations (more typically an hour). As a result, we are able to explore a wide range of parameters and study in detail the behaviour of the solutions as a function of the imposed forcing (boundary flows, differential rotation, magnetic field strength, etc.) and as a function of the background model (diffusivities, thermodynamical profile, etc.). This feature is invaluable when trying to understand how solutions scale with the various parameters – see GB08 for example. In addition, we always know that the solutions found are indeed the steady state solutions of the system, and not transients. On the other hand, taking into account transport by 3D turbulence is not possible (without artificial parameterization of its effects). In addition, we cannot a priori know whether the steady states found are stable, or whether they may be unstable to either 2D or 3D perturbations.

Interestingly, however, we can make use of the fact that the emergence of unstable solutions implies a reduction of the basin of attraction of the stable ones (see Section 3.4.2), and (tentatively) identify sudden convergence difficulties with the presence of a bifurcation. For example, the simulations of BZ06 can be compared with ours for

$$f_\nu = 2.6 \times 10^8,\ f_\eta = 8 \times 10^7 \text{ and } f_\kappa = 8 \times 10^5 \tag{27}$$

(see Section 4.1). Our numerical algorithm has little difficulty converging to a solution for parameters f_ν, f_η and f_κ, respectively, about two times larger than the ones quoted above. To go from there down to the values used by BZ06 on the other hand requires much more care, a problem which is very likely related to the fact that the BZ06 solution is seen to be mildly unstable to 2D and 3D perturbations.

4 NUMERICAL EXPERIMENTS

The versatility of the numerical algorithm constructed combined with its rapid real-time execution (see Appendix D) enables us to perform an extensive range of simulations, both in terms of the parameter regime studied and in terms of the forcing applied. In this section we use this tool in a number numerical experiments.

In Section 4.1, we first prove our diagnostic for the failure of previous numerical attempts (Paper I, BZ06) to reach a dynamical equilibrium qualitatively similar to the one studied by GM98. We reproduce a quasi-steady state similar to the one achieved by BZ06, and study its scaling properties. We show that the meridional flow velocities induced in the tachocline, when the radiative–convective interface is modelled as an impermeable boundary, are always too low to confine the field.

We contrast this result in Section 4.2 with a similar calculation in which meridional flows are directly pumped through the boundary (through some unspecified radial forcing mechanism). We show that their amplitude remains sufficiently high in the tachocline to provide significant field confinement.

We then perform a suit of simulations in Section 4.3, in the 'desirable' parameter regime specifically selected in Section 3.3.3, and discuss the numerically derived solutions both qualitatively and quantitatively. We show that the system can, in some situations and for low-enough diffusivities, achieve a balance qualitatively similar to that of the GM98 model, but that the solutions also reveal a number of previously unaccounted for dynamical subtleties (see Sections 4.4, 4.5 and 5.3).

4.1 Failure of 'impermeable' simulations

4.1.1 The calculation

In this first numerical experiment, we compare our quasi-steady solutions with those integrated by BZ06. Note that since the overall interior magnetic field strength decays slightly in their time-dependent calculations, while our steady state solutions fix the value of the field amplitude near the inner boundary, the two simulations can only be compared qualitatively at best. None the less, the comparison is meaningful since the system is thought to relax to a quasi-steady equilibrium on a time-scale comparable with the meridional circulation time-scale, which is argued (by BZ06) to be much shorter than the magnetic diffusion time-scale.

To achieve the same parameter regime as the one selected by BZ06 in terms of the diffusivities, we set

$$f_\nu = 2.6 \times 10^8\, \tilde{f},\ f_\eta = 8 \times 10^7\, \tilde{f} \text{ and } f_\kappa = 8 \times 10^5\, \tilde{f} \tag{28}$$

and progressively reduce $\tilde{f}$ from about 10^5 to 1. When $\tilde{f} = 1$, our diffusivities are the same in the tachocline region as theirs.[3] Naturally, we select $u_r^{\rm out} = 0$ to mimic an impermeable boundary as in BZ06. We also modify our bottom boundary conditions to be 'stress-free', again to be consistent with their simulations. Finally, the radial component of the magnetic field on the inner boundary is set to be same as the initial condition selected by BZ06 (i.e. $B_r = 500$ G at the poles at $r = r_{\rm in}$).

4.1.2 Qualitative comparison of the results

The results for $\tilde{f} = 1$ (see equation 28) are shown in Fig. 2. The overall structure of the streamlines and of the magnetic fields lines, as well as the amplitude of the toroidal field and of the differential

[3] Also note that the BZ06 simulations actually have constant diffusivities throughout the radiative interior, while ours vary with radius as in the Sun. Since we only seek a qualitative comparison of the two simulations, this difference in the diffusivities near the inner boundary is irrelevant.

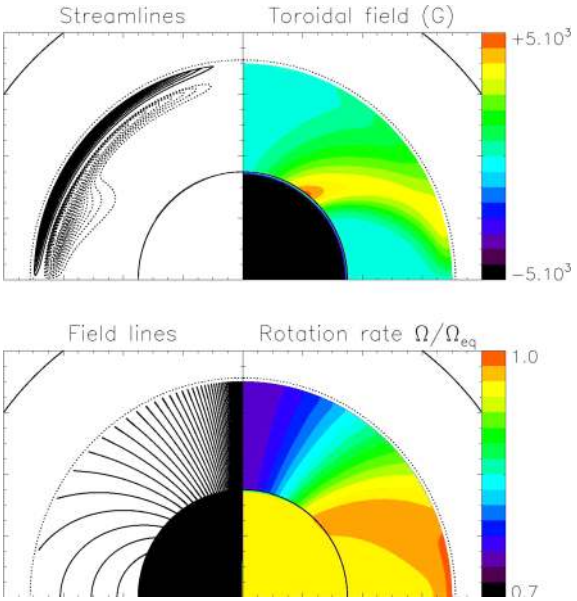

Figure 2. Quasi-steady state results for a numerical simulation similar to that of Brun & Zahn (see Section 4.1). In each quadrant, the dotted circle marks the position of the base of the convection zone at $r = r_{\rm cz}$, the outer solid circle marks the solar surface and the inner solid circle is at $r = r_{\rm in}$. Top left-hand panel: Streamlines of the meridional flow. Clockwise flows are shown as solid lines, and anticlockwise flows are shown as dotted lines. Top right-hand panel: Toroidal field (in gauss). Bottom left-hand panel: Magnetic field lines. Bottom right-hand panel: Angular velocity profile. Note how the magnetic field lines connect to the bottom of the convection zone and establish a differentially rotating Ferraro state throughout the domain.

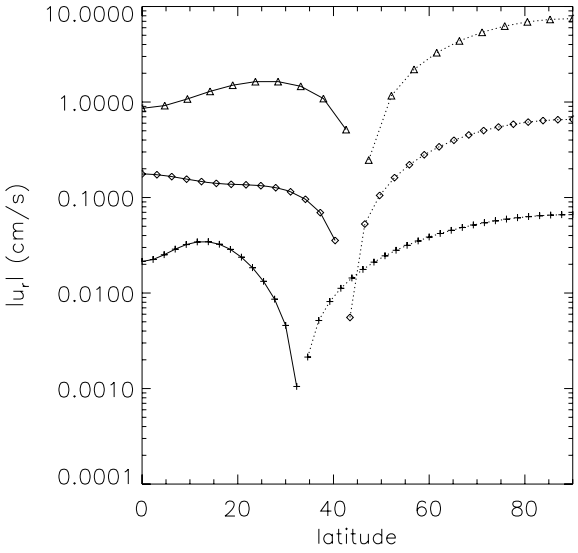

Figure 3. Absolute value of the radial component of the meridional flow at $r = 0.68\,{\rm R}_\odot$ as a function of latitude, when $\tilde{f} = 1$ (plus symbols), $\tilde{f} = 10$ (diamonds) and $\tilde{f} = 100$ (triangles), for $\tilde{f}$ defined in equation (28). The radial position was selected to be safely below the Ekman layer for all three calculations. The solid part of the curve denotes $u_r > 0$ and the dotted part of the curve denotes $u_r < 0$. Note how $|u_r|$ roughly scales with $\tilde{f}$.

rotation compare qualitatively well with the simulations of BZ06 (see the $t = 4.7$ Gyr solution in figs 4 and 5 of BZ06). Small discrepancies in the magnetic field geometry can be attributed to the fact that their magnetic field is diffusing out of their inner core, while it is maintained in our simulation by a permanent dipole.

This steady state calculation therefore confirms the main conclusion of the study carried out by BZ06, namely that in the case where the radiative–convective interface is modelled as an impermeable boundary, the only possible quasi-steady solution has an unconfined-field structure leading to a differentially rotating Ferraro state.

4.1.3 The nature and amplitude of the flows

We now justify our diagnostic of the failure of 'impermeable simulations' to find a confined-field solution. The induced meridional flows in this set of simulations are generated primarily by Ekman pumping on the boundary. Indeed, the magnetic field strength selected by BZ06 implies a field of the order of a few tens of gauss at the most near the outer boundary, and therefore according to the analysis of Section 3.3.3 a boundary layer in the Ekman regime rather than in the Hartmann regime. In that case, the flow amplitudes are in fact well estimated by the (non-magnetic) work of GB08 and scale as $E_\nu/\sqrt{Pr}$. This is verified in Fig. 3, which shows the radial velocity profile of the flows as a function of latitude, well below the Ekman layer (at $r = 0.68\,{\rm R}_\odot$), in three different simulations: for $\tilde{f} = 1$, 10 and 100. It is clear from the figure that the meridional flow velocity decreases linearly with $\tilde{f}$, and can in fact be shown to scale as predicted above.

As a result, one can straightforwardly see that the magnetic Reynolds number does not increase with decreasing E_η when the respective diffusivity ratios are held constant: with $R_{\rm m}$ defined as in equation (26), if $|u_r|$ is proportional to $\sqrt{f_\kappa f_\nu}$ then the magnetic Reynolds number is in fact proportional to $\sqrt{f_\nu f_\kappa}/f_\eta$ and remains roughly constant as $\tilde{f}$ decreases. The effective magnetic Reynolds number of the BZ06 simulations can be estimated from the flow amplitudes calculated in Fig. 3 to be $R_{\rm m} \sim 5 \times 10^{-3}$ – far too low to influence the magnetic field.

Using the true solar diffusivities would not change the situation since in that case it can be shown that the expected magnetic Reynolds number is of the order of $R_{\rm m} \sim 4 \times 10^{-2}$. We have therefore confirmed our original diagnostic, namely that the reason for the failure of numerical simulations to find confined-field solutions is not related to the fact that the diffusivities in the simulations are too high (i.e. selecting solar diffusivities would yield a similar result), but rather to a fundamental misrepresentation of the radiative–convective interface.

4.2 The possibility of magnetic field confinement by the thermoviscous mode

Following the original idea proposed by GM98, we now explore the possibility of confining the interior field through flows which are directly downwelling from the convection zone. As shown by GB08, flows which are pumped into and out of the radiative zone (by stresses in the convection zone for example) can retain significant amplitudes throughout much of the tachocline (and below), and could therefore result in a magnetic Reynolds number larger than unity for low enough diffusivities. We illustrate this idea with a qualitative example, which, for ease of comparison with the results of the previous section, is selected to have the same diffusivity ratios and magnetic field strength as those of BZ06.

4.2.1 *Structure of the imposed meridional flow*

We now select a radial velocity profile $u_r^{\rm out}(\theta)$ which satisfies the following properties: (i) $u_r^{\rm out}(0) = 0$ (the radial velocity is zero on the polar axis), and the flow is symmetric with respect to the equator (ii) the total mass flux through the boundary (at $r = r_{\rm cz}$) is zero:

$$\int_0^{\pi/2} u_r^{\rm out}(\theta) \sin\theta {\rm d}\theta = 0 \tag{29}$$

and (iii) the total angular momentum flux carried by the meridional circulation through the boundary is zero:

$$\int_0^{\pi/2} r^2 \sin^3\theta \tilde{\Omega}_{\rm cz}(\theta) u_r^{\rm out}(\theta) {\rm d}\theta = 0. \tag{30}$$

Note that we require u_r to vanish on the polar axis to suppress the emergence of a polar vortex. Indeed, a vortex is otherwise expected to form by angular momentum conservation when and where the downward flow is deflected away from the poles by the stratification of the radiative zone. Finally, also note that u_θ is naturally zero on the polar axis by construction (see Appendix C).

The simplest solution which satisfies these constraints is a 6th-order polynomial in $\mu = \cos(\theta)$:

$$u_r^{\rm out}(\mu) = U_0 \left(1 + \sum_{n=1}^{3} \alpha_n \mu^{2n}\right), \tag{31}$$

where

$$\begin{aligned}
\alpha_1 &= -\frac{3(715 + 169a_2 + 141a_4)}{143 + 13a_2 + 25a_4}, \\
\alpha_2 &= \frac{5(1001 + 299a_2 + 207a_4)}{143 + 13a_2 + 25a_4}, \\
\alpha_3 &= -\frac{91(33 + 11a_2 + 7a_4)}{143 + 13a_2 + 25a_4}
\end{aligned} \tag{32}$$

and U_0 is the radial velocity at the equator.

An example of this profile can be seen in Fig. 4: for the values of a_2 and a_4 given in (1) the upwelling region is centred at 30° latitude, and ranges from 15° to 45°. Note that the selection of this 'simplest' profile is fairly arbitrary: one may also wish instead to select a profile where the width and position of the upwelling region is prescribed, or require additionally that the equatorial velocity be zero, etc. The only necessary constraints, however, are zero mass and angular momentum fluxes. These conditions are often ignored, but are crucial to obtaining meaningful results. Failure to satisfy them yields unphysical angular velocity profiles with large radial gradients, since the amplitude of the viscous torque is then artificially inflated to compensate for the angular momentum flux carried by the flow (see Garaud 2007 and GB08).

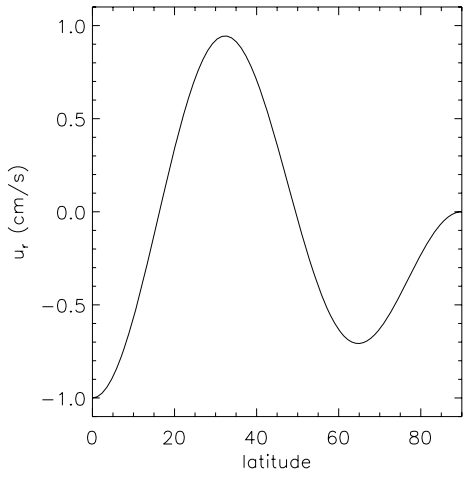

Figure 4. Example of imposed radial flow $u_r^{\rm out}$ as a function of latitude, for the values of a_2 and a_4 described in equation (1), satisfying the conditions listed in the main text. The velocity of the flow (U_0) here is arbitrarily selected to be -1 cm s^{-1} at the equator. The width of the upwelling region, as can be seen in the figure, spans about 30° in latitude and is centred on 30°.

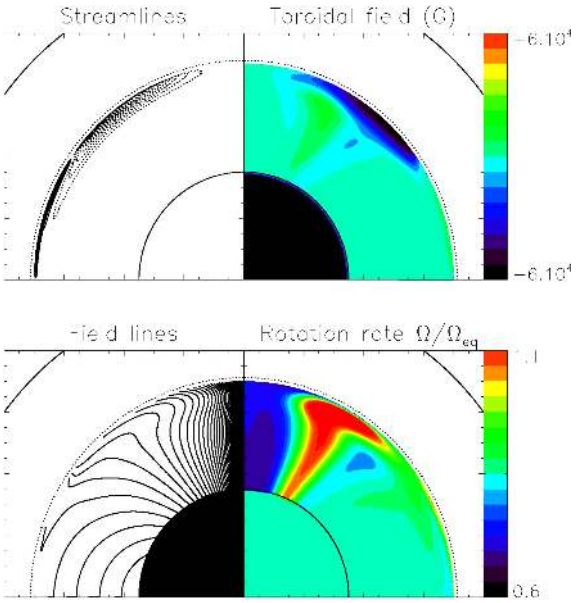

Figure 5. Same as Fig. 2, but with an imposed meridional flow at $r = r_{\rm out}$ (see Fig. 4).

4.2.2 *Qualitative structure of the solutions*

In the simulation presented here, the diffusivities are selected as in equation (28) with $\tilde{f} = 1$. A radial meridional flow profile is imposed at the outer boundary (see equation 31), with an amplitude U_0 of -5.5 cm s^{-1}. The resulting numerical solution is presented in Fig. 5. It clearly shows that the field lines are strongly distorted by the meridional flows, and seem to be confined both near the equator, and more importantly also near the poles. In fact, our results appear to be at least qualitatively similar to the analytical solutions of Wood & McIntyre (2007), which focused on the polar regions only. The angular velocity profile is very different from the one observed in the simulations shown in Fig. 2 and reveals uniform rotation from the equator up to about 60° in latitude. The rotation rate of the inner core is found to be $0.86\Omega_{\rm eq}$.

We have therefore shown that, at least on a qualitative basis, magnetic field confinement is possible provided a radial flow is imposed near the radiative–convective interface.

4.3 Exploration of parameter space

Having proved on a qualitative basis that the GM98 model may indeed lead to global field confinement, we now turn to a more quantitative analysis of the resulting tachocline dynamics. For this purpose, we return to using the boundary conditions discussed in Section 3.2.

In what will be referred to from here on as the 'fiducial model', the enhancements factors f_ν, f_η and f_κ are now selected as follows

to be in the 'desirable' parameter range discussed in Section 3.3.3:

$$f_\nu = \frac{\tilde{f}}{10},\ f_\eta = \tilde{f},\ f_\kappa = \frac{\tilde{f}}{100}, \tag{33}$$

and the factor $\tilde{f}$ is progressively reduced from 10^{15} down to 10^{10} typically (8×10^9 for the lowest case). For $\tilde{f} = 10^{10}$, and in the tachocline region, $E_\nu \sim 2 \times 10^{-6}$, $E_\eta \sim 3 \times 10^{-4}$ and $E_k \sim 10^{-1}$. In that case, and for all simulations, $Pr = 10Pr^\odot$ (guaranteeing that the thermoviscous mode length-scale is indeed of the order of the entire radiative zone), and $Pr_\mathrm{m} = 0.1Pr_\mathrm{m}^\odot$. Note that the simulations of BZ06 use a Prandtl number of the order of $300Pr^\odot$, which does not satisfy our criterion for the hierarchy of the expected characteristic length-scales.

The magnetic field strength on the inner boundary at the pole is selected to be $B_0 = 7$ T, so that the field strength in the tachocline would be of the order of 1 T in the absence of meridional flows. The radial flow velocity at the outer boundary is the one discussed in Section 4.2.1 with $U_0 = -550\,\mathrm{cm\ s^{-1}}$, and the latitudinal flow velocity is everywhere zero.

4.3.1 *From the diffusive regime towards the asymptotic regime*

The qualitative evolution of the poloidal field topology and of the angular velocity profile as $\tilde{f}$ is reduced can be seen in Fig. 6, while the corresponding figure for the streamlines and the temperature profile is Fig. 7. In all simulations, the viscous Ekman number is much smaller than 1. The magnetic field begins to affect the angular velocity profile as $\tilde{f}$ decreases from 10^{13} to 10^{12}, notably in the deeper interior.[4] This transition occurs when the magnetic Ekman number drops below 1. The structure of the temperature perturbation profile changes as $\tilde{f}$ is decreased from 10^{12} down to 10^{11}, which is attributed this time to the 'thermal' Ekman number approaching 1. Finally, there is a clear transition between the 'unconfined-field' configuration for $\tilde{f} = 10^{11}$ and the 'confined-field' configuration for $\tilde{f} = 10^{10}$, which corresponds to the magnetic Reynolds number increasing to values above unity.

Contrary to the impermeable-boundary case studied by BZ06, the radial flow velocities do not decrease with the diffusivities, but are actually seen to increase as $\tilde{f}$ is reduced. This is illustrated in Fig. 8, which shows the radial flow velocity near the base of the presumed tachocline (at $r = 0.68\,\mathrm{R}_\odot$, as in Fig. 3), as a function of latitude, for three values of $\tilde{f}$. Provided $E_\kappa < 1$, it appears that $\tilde{u}_r \propto 1/\tilde{f}$ although this scaling cannot, for numerical reasons, be explored over many orders of magnitude. As a result, the non-linear interaction of the flow and the field rapidly becomes stronger and the field appears to be more and more confined, as can be seen in the last panel of Fig. 6.

4.3.2 *The 'lowest diffusivities' simulation*

We now decrease $\tilde{f}$ as far as possible, until convergence becomes too difficult. The lowest value achieved in the fiducial model is $\tilde{f} = 8 \times 10^9$ and the results are presented in Fig. 9. The number of radial meshpoints used is 3000, and the number of latitudinal modes is 80 (note that since only even modes are selected to guarantee equatorial symmetry, solving for 80 modes means that the highest Fourier mode considered actually is cos (158 θ), see Appendix C).

[4] Recall that the magnetic diffusivity is smaller in the deeper interior, see Appendix A.

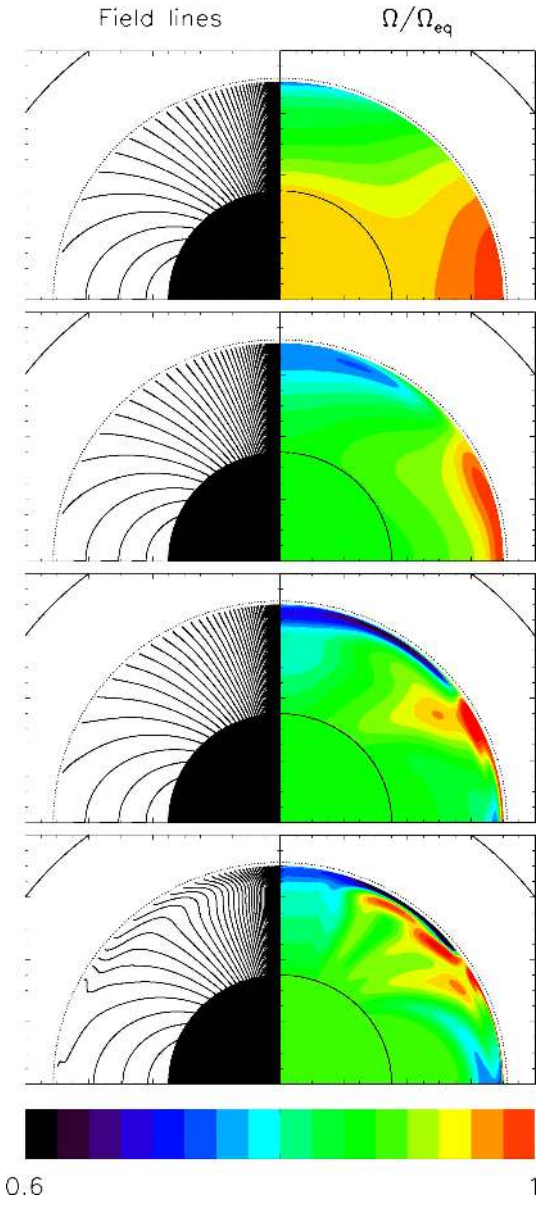

Figure 6. Evolution of the poloidal field topology and of the angular velocity profile in the fiducial model for, from top to bottom, $\tilde{f} = 10^{13}$, 10^{12}, 10^{11} and 10^{10}. Note that regions with $\Omega < 0.6\Omega_\mathrm{eq}$ are drawn in black.

The top right-hand quadrant of Fig. 9 shows representative streamlines. The Ekman layer near the outer boundary, of width $\sim 0.001\,\mathrm{R}_\odot$, is just visible in the top right-hand strip. The Ekman layer flow does indeed downwell at the poles and equator, and upwells in mid-latitudes.

More clearly visible is the 'thermoviscous' mode below the Ekman layer, which has the opposite structure[5]: downwelling in mid-latitudes and upwelling near the poles and equator. This mode appears to be confined roughly within $r \in [0.67, 0.7]\,\mathrm{R}_\odot$, an effect which can only be attributed to the Lorentz forces arising from

[5] This can be attributed to the perfectly conducting conditions on the temperature; a zero perturbed flux condition on the other hand yields a thermoviscous mode circulating in the same direction as the imposed flow, see GB08.

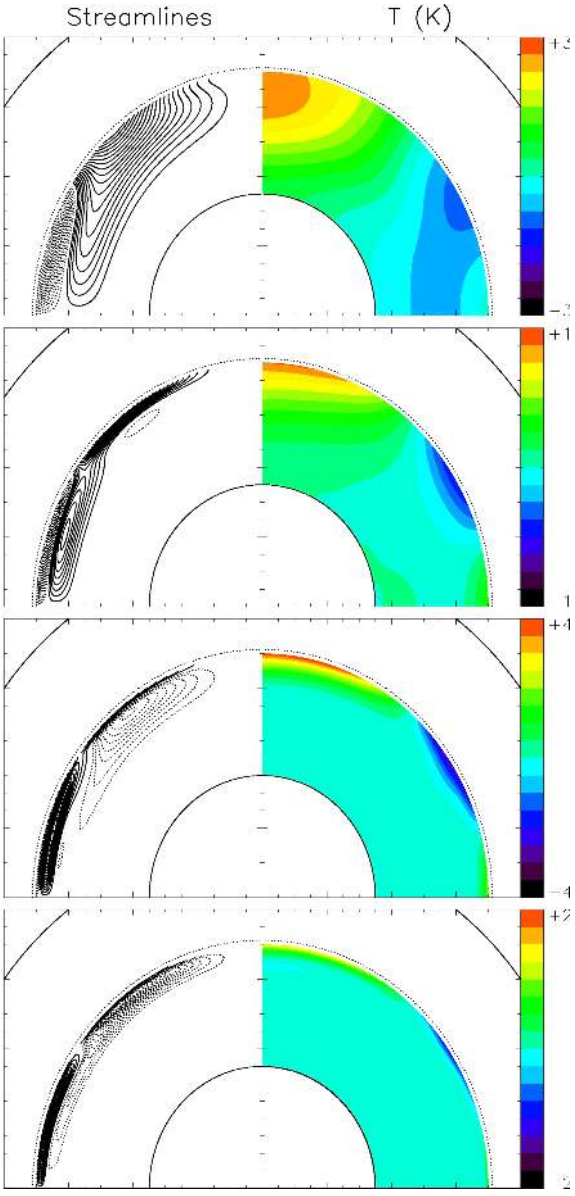

Figure 7. Evolution of the topology of the streamlines and of the temperature perturbations in the fiducial model for, from top to bottom, $\tilde{f} = 10^{13}$, 10^{12}, 10^{11} and 10^{10}. Note that the streamlines shown are representative streamlines, the contours selected are different in each plot. Also note that the temperature scale is different in each plot.

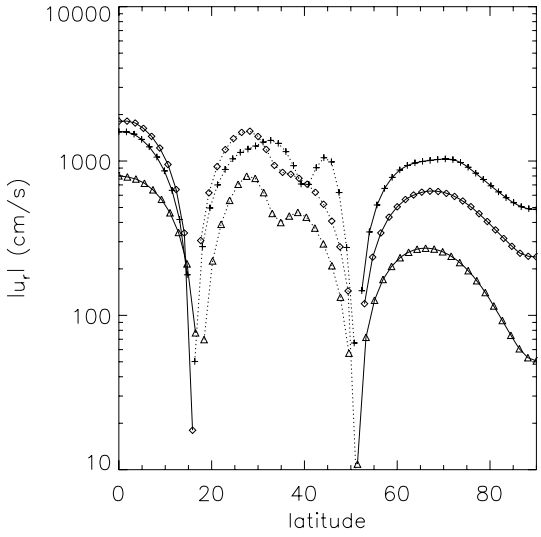

Figure 8. Radial flow velocities at $r = 0.68\,R_\odot$ as a function of latitude in the fiducial model, for three values of $\tilde{f}$: $\tilde{f} = 10^{10}$ (plus symbol), $\tilde{f} = 3 \times 10^{10}$ (diamonds) and $\tilde{f} = 10^{11}$ (triangles). As in Fig. 3, the solid lines denote upward flow ($\tilde{u}_r > 0$) and the dotted lines denote downward flow ($\tilde{u}_r < 0$). The figure therefore shows a downwelling in mid-latitude, with upwelling at the poles and the equator. Note how the amplitude of the radial velocity appears to increase with decreasing $\tilde{f}$.

the magnetic field underneath. Indeed, the solutions of GB08 in the absence of magnetic fields in the same parameter regime do not reveal any structure on this typical length-scale. The associated effect of the flow in confining the magnetic field is also obvious in the bottom left-hand quadrant: the field lines are most strongly distorted away from the strictly dipolar structure in the same region ($r \in [0.67, 0.7]\,R_\odot$). Field confinement is discussed in more detail in Section 4.4.

The solution for the angular velocity profile is again more complex than expected: the combination of the two modes of propagation of the meridional flows creates radial structures both on the Ekman scale and on a larger scale ($r \sim 0.1\,R_\odot$), as well as latitudinal structures which are clearly seen to be correlated with the magnetic field lines. However, contrary to the solution shown in Fig. 2, there is no clear evidence for a *large-scale* latitudinal or radial gradient in Ω below about $0.6\,R_\odot$, including in the polar regions. This is the first set of self-consistent simulations to reveal this kind of solution. Since the angular velocity profile inferred from helioseismic inversions can be thought of as a weighted spatial average of the true angular velocity profile in the Sun, and since the spatial extent of the averaging kernels is much larger than the features seen in the simulations, the angular velocity profile shown in Fig. 9 would be observationally interpreted to be uniform below $0.6\,R_\odot$, whereas the one shown in Fig. 2 would not. The actual value of the rotation rate calculated in the simulations is discussed in Section 4.5.

A closer look at the angular velocity profile in the region $r \in [0.65, 0.7]\,R_\odot$ (see the bottom right-hand strip) reveals a change in the dominant angular momentum transport processes between the uppermost layers ($r > 0.67\,R_\odot$) and the lower layers ($r < 0.67\,R_\odot$). When $r > 0.67\,R_\odot$ the angular velocity contours are more or less aligned with the streamlines, whereas for $r < 0.67\,R_\odot$ the angular velocity contours are aligned with the magnetic field lines. This is at least qualitatively consistent with the idea proposed by GM98 of a multilayered tachocline, in which the dynamics of the uppermost layer are controlled by the tachocline flows, while the dynamics of the bulk of the radiative zone are controlled by the primordial field. The interface between the two regions, which could be identified with the 'magnetic diffusion layer' of the GM98 model, clearly has quite a complex topology.

One can also observe a number of very strong localized 'jets' of more rapidly or more slowly rotating fluid. The jets appear to be stronger for lower diffusivities (one can easily compare the results of Fig. 9 with the last panel of Fig. 6). In fact, we tentatively attribute the numerical scheme's failure to find solution for $\tilde{f} < 8 \times 10^9$ to an intrinsic instability of the jets. But whether such strong features would exist in the Sun is debatable: both the imposed flow velocities and the magnetic field strength have been artificially increased by many orders of magnitude to ensure a magnetic Reynolds number greater than one in the simulations, and a Hartmann number closer

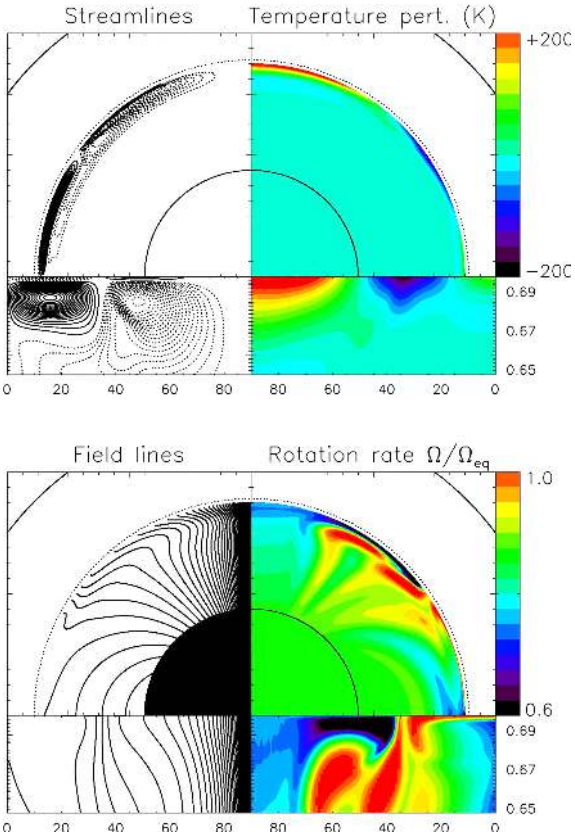

Figure 9. Results of the simulations of the fiducial model for $\tilde{f} = 8 \times 10^9$. For each quantity plotted (from top left-hand to bottom right-hand sides, respectively, representative streamlines, temperature perturbations, field lines and rotation rate), we show both a full quadrant as well as a zoomed-in strip of outer boundary layer (the region between $r = 0.65\,\mathrm{R}_\odot$ and $r = r_{\rm out}$). As usual, the solid streamlines denote clockwise flows, and dotted streamlines denote counterclockwise flows. Note that regions with $\Omega < 0.6\,\Omega_{\rm eq}$ are drawn in black.

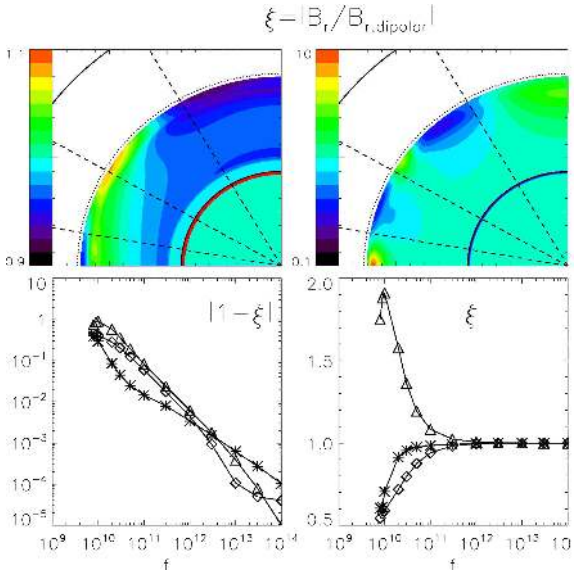

Figure 10. Measure of magnetic confinement, using the quantity ξ as defined in the main text, Section 4.4. Top left-hand panel: Variation of ξ with radius and latitude, in a fiducial model for $\tilde{f} = 10^{11}$. Top right-hand panel: Same as on the left-hand panel but for $\tilde{f} = 8 \times 10^9$. Note the change in the scale of the perturbations between the two plots, and also note that here the contours are logarithmically spaced. Bottom left-hand panel: $|1 - \xi|$ evaluated at the outer boundary, at three different latitudes, respectively, in the downwelling regions (10°, plus symbols, and 60°, diamonds) and in the middle of the upwelling region (30°, triangles). This log–log plot emphasizes the power-law relationship between $|1 - \xi|$ and $\tilde{f}$ for $R_{\rm m} < 1$, see main text. Bottom right-hand panel: Similar to the left-hand plot but showing ξ with a linear scale, emphasizing the breakdown of this relationship when $R_{\rm m} > 1$.

to that of the Sun (see Section 3.3.3). As a result, the amplitude of these jets is also artificially increased in the simulations compared with what one may expect in the Sun. Unfortunately, given the non-linear nature of the problem, it is difficult to predict what the actual strength of these jets would be should diffusivities, magnetic field and imposed flows velocities be simultaneously reduced to the expected solar values.

4.4 Magnetic field confinement

To study the nature of field confinement more quantitatively, we consider the ratio $\xi = |B_r/B_{r,\rm dipolar}|$ where $B_{r,\rm dipolar}$ is the hypothetical radial component of the solution for the magnetic field in the purely diffusive case:

$$B_{r,\rm dipolar}(r,\theta) = B_0 \cos\theta \left(\frac{r}{r_{\rm in}}\right)^{-3}. \qquad (34)$$

Typically, we expect that $\xi < 1$ when magnetic field lines are either completely expelled from a region, or bent to the horizontal. On the other hand, we expect that $\xi > 1$ in regions where the magnetic field lines are pushed together by converging (latitudinal) flows. It is therefore a good diagnostic of the processes we are interested in.

The quantity ξ is shown in Fig. 10 for various simulations. The top two quadrants are derived from the numerical solutions for $\tilde{f} = 10^{11}$ and 8×10^9, respectively, and reveal a strong change in the behaviour of the solutions when $R_{\rm m} < 1$ and $R_{\rm m} > 1$.

In the case where $\tilde{f} = 10^{11}$, we observe a good match between the spatial variation of ξ and the imposed forcing: $\xi < 1$ in downwelling regions and $\xi > 1$ in the upwelling regions (at mid-latitudes). However, the amplitude of ξ remains close to 1, revealing only a very weak effect of the flow on the field. This is not entirely surprising since the magnetic Reynolds number for $\tilde{f} = 10^{11}$ can be deduced from the flow amplitude shown in Fig. 8 to be $R_{\rm m} \sim 0.03$ at $r = 0.68\,\mathrm{R}_\odot$. In fact, in this very weakly non-linear regime there is some evidence for a correlation (see Fig. 10, bottom left-hand quadrant) between $1 - \xi$ and $\tilde{f}$: we find that $|1 - \xi| \sim 10^{10}\,\tilde{f}^{-1}$.

However, Fig. 10 also reveals that matters become more complex as $R_{\rm m}$ increases above unity. For $\tilde{f} = 8 \times 10^9$ the magnetic Reynolds number is now of the order of $R_{\rm m} \simeq 1.5$, and the connection between the field and the meridional flow is correspondingly fully non-linear. The correlation between $1 - \xi$ and $\tilde{f}$ breaks down, as seen in the bottom right-hand quadrant. This incidentally proves that the kind of boundary conditions advocated by Kitchatinov & Rüdiger (2006) to mimic 'field confinement by meridional flows' cannot accurately describe the non-linear dynamics of the system. We also observe that the regions of enhancement and reduction of the radial field are no longer perfectly correlated with the *imposed* upwelling/downwelling regions. In fact, some enhancement in the radial field strength can be seen near the equator as well as near the polar regions. This can be attributed to the convergence points of the meridional flows *below* the Ekman layer, which, as seen in Fig. 9 have the opposite sign as that of the imposed flow.

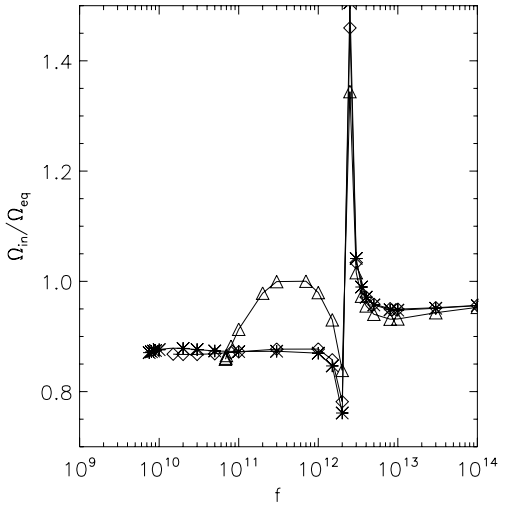

Figure 11. Angular velocity of the inner core as a function of $\tilde{f}$, in the fiducial model (star symbols), and in a model where the amplitude of the imposed radial flow is 10 times larger (triangular symbols) and 10 times smaller (diamond symbols), respectively.

All in all, although there is definite evidence for magnetic field confinement along the lines of the model proposed by GM98, it is probably fair to say that the system behaves in a far more complex way than anticipated, and that the simulations in the fiducial model are just beginning to scratch the surface of the 'interesting' regime.

4.5 Interior angular velocity

As in Paper I, we consider the angular velocity of the inner core $\Omega_{in} = \overline{\Omega} + \tilde{\Omega}_{in}$ (which is an eigenvalue of the calculation performed) as a diagnostic of the most important angular momentum transport processes, and of the 'accuracy' of the model in reproducing the observations. This quantity is shown in Fig. 11 as a function of $\tilde{f}$ for the fiducial model, and for simulations with faster and slower imposed flows.

In very diffusive simulations, the predicted angular velocity $\Omega_{in} \simeq 0.959\ \Omega_{eq}$ is consistent with purely viscous angular momentum transport throughout the entire interior (see Gough 1985). As $\tilde{f}$ is progressively reduced, the system undergoes a rather impressive bifurcation at $\tilde{f} \simeq 2.5 \times 10^{12}$, which corresponds to the change of nature of the boundary layer near the inner core from an Ekman layer to an Ekman–Hartmann layer. When this happens, a new flow cell of opposite vorticity appears right against the inner core, so that angular momentum transport changes direction. This leads to a rather dramatic jump in the inner core rotation rate, which is unlikely to be of any relevance to the Sun, but deserved an explanation. Note that the critical value of $\tilde{f}$ for which the bifurcation occurs is proportional to the imposed magnetic field strength B_0.

In the case of the fiducial model, the angular velocity of the core then remains roughly constant [$\Omega_{in} \simeq (0.875 \pm 0.005)\Omega_{eq}$] as $\tilde{f}$ is further reduced by two orders of magnitude. This range corresponds to the regime where $R_m < 1$, where the magnetic field lines essentially remain dipolar. In fact, the same inner core velocity is also found for lower imposed flow velocities (see Fig. 11), as well as for higher and lower field strength (always with $R_m < 1$). This suggests that the value $\Omega_{in} \sim 0.875\Omega_{eq}$ is a rather universal characteristic of angular momentum transport by dipolar fields in the Hartmann regime, in this particular geometry, and subject to this particular set of boundary conditions.[6]

However, it is clear from the analysis of Section 4.4 that the simulations in the fiducial model have not quite yet reached the asymptotic regime even for the lowest values of $\tilde{f}$ achieved. As a matter of fact, in the last few points of the fiducial model curve (in the region where R_m begins to exceed 1), Ω_{in} is seen to change more rapidly, decreasing slightly below $0.87\Omega_{eq}$.

The role of the meridional flows as angular momentum transporters can best be seen in a simulation with much higher imposed flow velocities (see the curve with the triangular symbols, for $U_0 = -5500\,\mathrm{cm\,s^{-1}}$). In these simulations, the transition to $R_m > 1$ occurs for values of $\tilde{f}$ typically 10 times larger than in the fiducial model. In that case, we observe that the predicted core velocity is notably different from the other two cases, and changes rather rapidly with $\tilde{f}$. It is therefore more than likely that the predicted angular velocity of the core in the fiducial model would also begin to deviate more noticeably away from $\Omega_{in} = 0.875\,R_\odot$ were we able to continue decreasing $\tilde{f}$. Again, we are only beginning to approach the asymptotic regime so that the simulated angular velocity of the core cannot yet and should not be compared directly with that of the Sun.

5 DISCUSSION AND PROSPECTS

5.1 Summary of the results

Despite the difficulties encountered when attempting to find numerical solutions for asymptotically low values of the diffusivities, the non-linear dynamics which emerge from our simulations are closer to what one may expect from the GM98 model than any other simulation performed to date.

More precisely we do observe (see Section 4.3) the quenching of the large-scale differential rotation by the primordial magnetic field, even in the polar regions. We also observe the partial confinement of the field by the meridional flows to the radiative interior (see Section 4.4), with the reduction of the radial field strength (in some regions) by more than 70 per cent. Finally, we observe the concurrent confinement of the meridional flows to the upper layers of the radiative zone ($r > 0.67\,R_\odot$) by the magnetic field. We have not yet been able to reduce the diffusivities down sufficiently far to observe a truly segregated structure where the bulk of the tachocline flows are completely magnetic-free. However, there is evidence in the observed rotation profile (see Fig. 9) for a transition between regions where angular momentum transport is dominated by the meridional flows, and regions where it is dominated by the magnetic field. The 'magnetic diffusion layer' studied by GM98, which is thought to control this transition, appears to have a rather complex geometrical structure which prevents a more detailed study of the GM98 scalings.

The calculated value of the interior angular velocity Ω_{in} (see Section 4.5), using the boundary conditions discussed here, does not match the observed value. However, since even the lowest diffusivity simulations presented are only just beginning to enter the asymptotic parameter regime described in Section 3.3.3 we do not view the poor match with the observations as an intrinsic problem with the GM98 model (yet) but rather as evidence that more work should be done to decrease the diffusivities even further – a challenging task.

[6] Interestingly, a value much closer to the observations can be obtained merely by using different boundary conditions on the toroidal field at $r = r_{in}$. This result will be presented in more detail in a forthcoming paper.

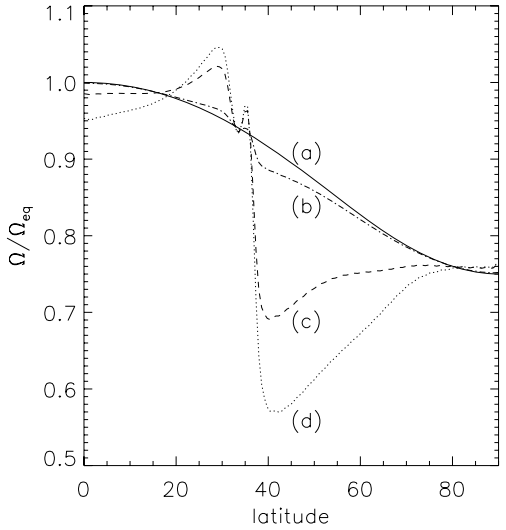

Figure 12. Angular velocity profile on and just below the radiative–convective interface (a) at $0.7\,R_\odot$, (b) at $0.6999\,R_\odot$, (c) at $0.6995\,R_\odot$ and (d) at $0.699\,R_\odot$ in the fiducial model for $\tilde{f} = 8 \times 10^9$. Note how the angular velocity profile in (and therefore also below) the Ekman layer is very different from the one imposed by the convection zone.

5.2 The stability of the solutions

As described in Section 4.3, the convergence of the solutions becomes rather difficult when the values of the diffusivities are decreased below a certain threshold (in the fiducial model for $\tilde{f} < 8 \times 10^9$). The typical reasons for this convergence failure were listed and discussed in Section 3.4.2: intrinsic linear/non-linear instabilities or insufficient latitudinal resolution. In this particular case, the various scenarios are equally plausible, and difficult to disentangle without a supporting fully non-linear 3D calculation. The field configuration near the inner core could be subject to instabilities (as seen in the simulations of BZ06). The Ekman(–Hartmann) layer near the outer boundary could also be subject to instabilities, or could be developing latitudinal structures which are too fine to resolve (see Fig. 12). We have in fact tentatively identified the emergence of strong jets in the angular velocity profile (see Fig. 9 for example) as the most likely source of instabilities (and convergence failure), but the reader should be cautioned that this statement is only speculative.

As mentioned in Section 4.3, whether the equilibrium governed by the GM98 model is stable or unstable cannot directly be inferred from the stability of the numerical solutions (since they operate in a different parameter regime) but it is clearly a fundamental question. Should our diagnostic concerning the stability of the jets prove to be correct, then a possible path for future investigation (using this relaxation method) may be to continue searching for solutions, starting where we left off, and slowly lowering simultaneously the amplitude of the imposed flow (and field) with the diffusivities to limit the strength of the jets generated. This could be seen as blindly navigating the stable regions of parameter space while avoiding instability reefs. But what could ideally be derived from such an exercise, should we be able to acquire sufficient data, are scaling relationships between the jet strength, the diffusivities and the imposed flow strength which may then be used to infer tentative information on the stability of the GM98 solution itself.

5.3 The role of an Ekman layer

Our simulations have also revealed a fundamental difference with the original GM98 model: the presence and role of an Ekman mode.[7] While it is clear from Fig. 9 that the Ekman flows themselves play no role in confining the field (contrary to the claims made by Kitchatinov & Rüdiger 2006) our simulations reveal that the role of the Ekman layer is still far from trivial.

Indeed, the differential rotation profile imposed at the radiative–convective interface is quite different from the differential rotation profile transmitted by the Ekman layer. This is illustrated in Fig. 12, which shows the evolution of the angular velocity profile with depth across the Ekman layer. Thus while the GM98 model correctly describes the non-viscous tachocline dynamics *below* the Ekman layer, the Ekman mode could in fact influence the system by modifying the angular velocity profile 'seen' by the bulk of the tachocline.[8]

The extent to which this effect influences the tachocline is unclear. First, other processes which also transport angular momentum (convective overshoot, gravity waves, small- and large-scale magnetic stresses associated with the dynamo field) are known to take place in the close vicinity of the radiative–convective interface. These processes were not included in GM98's analysis and cannot be modelled with the present numerical algorithm, but could equally affect the tachocline dynamics. Secondly, Ekman layers (laminar or turbulent) must *by definition* be present in any rotating system which exhibits very rapid changes in the imposed stresses. However, whether the Ekman mode actually plays an important role in the tachocline dynamics depends on the relative importance of the bulk thermal-wind stresses and the combination of all the other rapidly varying turbulent stresses (see Fig. 13). Indeed, if the base of the convection zone is already essentially in thermal-wind balance (see Miesch 2005 for instance), then the amplitude of the Ekman mode and its effect on the angular velocity profile will be small (GB08). On the other hand, if this is not the case then significant Ekman flows are expected (as in the simulations shown in the present work for example), with the aforementioned consequences.

5.4 Prospects

The present work has emphasized the importance of flows downwelling from the solar convection zone as a means to confine the internal primordial field below the bulk of the tachocline – and in particular below the region where the dynamo field is thought to be generated – and guarantee the uniform rotation of the radiative interior, as discussed by GM98. The nature of the thermal and dynamical balance governing the convection zone itself therefore also controls the dynamics of the tachocline through the spatial variation and amplitude of the flows crossing the radiative–convective interface. Meanwhile, steady progress in modelling the convection zone has emphasized its dependence on the thermal stratification of the tachocline (Rempel 2005; Miesch, Brun & Toomre 2006). One can only conclude that the dynamics of the convective and radiative regions are intrinsically and fundamentally coupled through this internal layer called the tachocline, and that the only sensible way forward from this point on is the construction of whole-Sun models including both regions.

[7] Since the bulk of the GM98 tachocline is presumed to be magnetic-free, one should indeed consider an Ekman mode rather than an Ekman–Hartmann mode.

[8] Adding another layer to the sandwich.

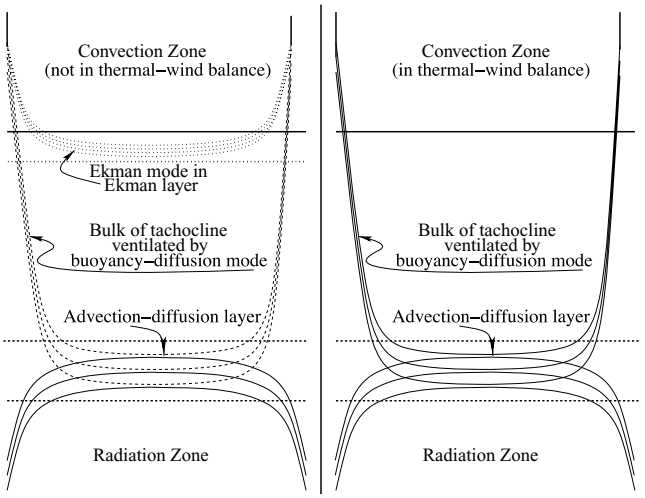

Figure 13. A pictorial representation of the expected tachocline flows in two extreme cases. In both pictures, flows are downwelling from the convection zone into the radiative zone. As in the GM08 model, the bulk of the tachocline is ventilated by the thermoviscous mode, which interacts with the magnetic field in a thin advection–diffusion layer. On the left-hand side, and as in the simulations presented in this paper, the convection zone is not dominated by thermal-wind balance, and a significant portion of the flows downwelling from the convection zone rapidly return within a thin Ekman layer. The angular velocity profile seen by the tachocline differs from the one observed in the convection zone. On the right-hand side, a hypothetical situation where the convection zone is essentially in thermal-wind balance. In that case, the Ekman mode is negligible and the GM98 model directly applies.

ACKNOWLEDGMENTS

This work is the outcome of nearly ten years of discussions with many colleagues, including Nic Brummell, Sacha Brun, Céline Guervilly, Gary Glatzmaier, Douglas Gough, Michael McIntyre, Michael Proctor, Tamara Rogers, Nigel Weiss, Toby Wood, Jean-Paul Zahn. PG thanks them all for their patience. Respective parts of this work have been supported, at various times, by New Hall (Cambridge), PPARC, and more recently by Calspace (for J-DG) and by NSF-AST-0607495 (for PG). The numerical simulations were performed on the Pleiades cluster at UCSC, purchased using an NSF-MRI grant.

REFERENCES

Acheson D. J., Hide R., 1973, Rep. Prog. Phys., 36, 159
Brown T. M., Christensen-Dalsgaard J., Dziembowsky W. A., Goode P., Gough D. O., Morrow C. A., 1989, ApJ, 343, 526
Brun A. S., Zahn J.-P., 2006, A&A, 457, 665 (BZ06)
Brun A. S., Miesch M. S., Toomre J., 2004, ApJ, 614, 1073
Christensen-Dalsgaard J., Schou J., 1988, in Domingo V., Rolfe E. J., eds, ESA-SP286, Seismology of the Sun and Sun-Like Stars. ESA, Noordwijk, p. 149
Christensen-Dalsgaard J. et al., 1996, Sci, 272, 1286
Clune T. L., Elliott J. R., Miesch M. S., Toomre J., Glatzmaier G. A., 1999, Parallel Comput., 25, 361
Dziembowski W. A., Goode P. R., Libbrecht K. G., 1989, ApJ, 337, L53
Eddington A. S., 1925, Observatory, 48, 73
Elliott J. R., Gough D. O., 1999, ApJ, 516, 475
Ferraro V. C. A., 1937, MNRAS, 97, 458
Garaud P., 2001, University of Cambridge, PhD thesis
Garaud P., 2002, MNRAS, 329, 1 (Paper I)
Garaud P., 2007, in Hughes D. W., Rosner R., Weiss N. O., eds, The Solar Tachocline. Cambridge Univ. Press, Cambridge, p. 147
Garaud P., Brummell N. H., 2008, ApJ, 674, 498 (GB08)
Garaud P., Garaud J.-D., 2007. AMS Technical Report ams2007-17, available from http://www.ams.ucsc.edu/research.html
Gilman P. A., Morrow C. A., Deluca E. E., 1989, ApJ, 338, 528
Glatzmaier G. A., 1984, J. Comput. Phys., 55, 461
Golub G. H., Ortega J. M., 1993, Scientific Computing: An Introduction with Parallel Computing. p. 302
Gough D. O., 1985, in Rolfe E., Battrick B., eds, Proc. ESA Workshop, ESA, Noordwijk
Gough D. O., 2007, in Hughes D. W., Rosner R., Weiss N. O., eds, The Solar Tachocline. Cambridge Univ. Press, Cambridge, p. 3
Gough D. O., McIntyre M. E., 1998, Nat, 394, 755 (GM98)
Kitchatinov L. L., Rüdiger G., 2006, A&A, 453, 329
Kosovichev A. G., 1988, Sov. Astron. Lett., 14, 145
Miesch M. S., 2005, LRSP, 2, 1
Miesch M. S., Elliott J. R., Toomre J., Clune T., Glatzmaier G. A., Gilman P. A., 2000, ApJ, 532, 596
Miesch M. S., Brun A. S., Toomre J., 2006, ApJ, 641, 618
MacGregor K. B., Charbonneau P., 1999, ApJ, 519, 911
Mestel L., 1953, MNRAS, 113, 716
Mestel L., Weiss N. O., 1987, MNRAS, 226, 123
Press W. J., Teukolsky S. A., Vetterling W. T., Flannery B. P., 1996, Numerical Recipes in FORTRAN 77, 2nd edn. Cambridge Univ. Press, Cambridge, p. 753
Rempel M., 2005, ApJ, 622, 1320
Rüdiger G., Kitchatinov L. L., 1997, Astron. Nachr., 318, 273
Schou J. et al., 1998, ApJ, 505, 390
Spiegel E. A., Zahn J.-P., 1992, A&A, 265, 106 (SZ92)
Sule A., Rüdiger G., Arlt R., 2005, A&A, 437, 1061
Sweet E., 1950, MNRAS, 110, 548
Wood T. S., McIntyre M. E., 2007, in Stancliffe R. J., Dewi J., Houdek G., Martin R. G. and Tout C. A., eds, AIP Conf. Proc., Vol. 948, Unsolved Problems in Stellar Physics. Am. Inst. Phys., New York, p. 303
Wright S. J., 1992, SIAM J. Sci. Stat. Comput., 13, 742

APPENDIX A: SELECTION OF THE BACKGROUND STATE

The spherically symmetric background solar model selected for this paper is Model S of Christensen-Dalsgaard et al. (1996). Model S provides calculated solar data for all of the relevant thermodynamical and compositional quantities on a fixed mesh. In particular, we use the provided fields $\overline{T}$, $\overline{p}$, $\overline{\rho}$, $\overline{g}$, $\overline{N}^2$ (where N is the buoyancy frequency), $\overline{c}_{\rm p}$ and $\overline{\kappa}_{\rm R}$ (where $c_{\rm p}$ is the specific heat at constant pressure, and $\kappa_{\rm R}$ is the Rosseland mean opacity). In order to use these data for our purpose, we need to interpolate it upon our own selected numerical mesh, using a standard rational interpolation routine (cf. Numerical Recipes). The task is delicate since any 'roughness' in the interpolated functions results in failure of convergence of the numerical algorithm, and the two numerical meshes are intrinsically non-uniform: Model S has meshpoints strongly concentrated near the solar surface, near $r = 0$ and at the base of the convection zone $r_{\rm cz} = 0.713\,{\rm R}_\odot$, while our numerical mesh has meshpoints strongly concentrated near the domain boundaries $r_{\rm in}$ and $r_{\rm out}$. A new interpolating routine was created which automatically selects a certain number of points from the original mesh, performs the rational interpolation upon the desired mesh, and checks for the smoothness of the interpolated function and of its derivative. Should the result be inadequate, the procedure is repeated with a different set of target points. Selected background quantities are shown in Fig. A1.

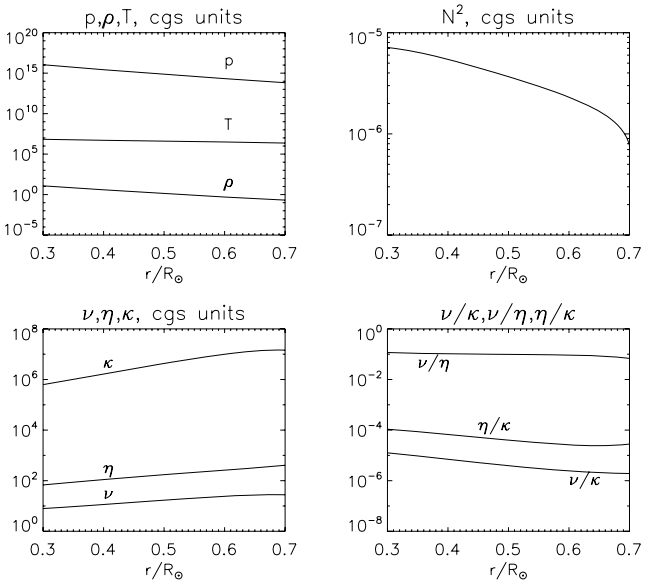

Figure A1. Background pressure, density and temperature (top left-hand corner), buoyancy frequency squared (top right-hand corner), microscopic diffusivities (bottom left-hand corner) and ratio of diffusivities (bottom right-hand corner) from Model S of Christensen-Dalsgaard et al. (1996).

The quantities $\overline{\nu}$, $\overline{\eta}$ and $\overline{k}$ are not provided by Model S, and must instead be calculated using the formulae derived by Gough (2007):

$$\overline{\nu}(r) = \nu_{\rm cz}\left[0.1\left(\frac{\overline{T}}{T_{\rm cz}}\right)^4\left(\frac{\overline{\rho}}{\rho_{\rm cz}}\right)^{-2}\left(\frac{\overline{\kappa}_{\rm R}}{\kappa_{\rm R,cz}}\right)^{-1}, + 0.9\left(\frac{\overline{T}}{T_{\rm cz}}\right)^{5/2}\left(\frac{\overline{\rho}}{\rho_{\rm cz}}\right)^{-1}\left(\frac{\ln\overline{\Lambda}}{\ln\Lambda_{\rm cz}}\right)^{-1}\right],$$
$$\overline{\eta}(r) = \eta_{\rm cz}\left(\frac{\overline{T}}{T_{\rm cz}}\right)^{-3/2}\left(\frac{\ln\overline{\Lambda}}{\ln\Lambda_{\rm cz}}\right),$$
$$\overline{k}(r) = \overline{\rho}c_{\rm p}\overline{\kappa}(r), \qquad \text{(A1)}$$

where the Coulomb logarithm $\ln\overline{\Lambda}$ and the thermal diffusivity $\overline{\kappa}$ are given by

$$\overline{\Lambda}(r) = \Lambda_{\rm cz}\left(\frac{\overline{\rho}}{\rho_{\rm cz}}\right)^{-1/2}\left(\frac{\overline{T}}{T_{\rm cz}}\right)^{3/2},$$
$$\overline{\kappa}(r) = \kappa_{\rm cz}\left(\frac{\overline{T}}{T_{\rm cz}}\right)^{3}\left(\frac{\overline{\rho}}{\rho_{\rm cz}}\right)^{-2}\left(\frac{\overline{\kappa_{\rm R}}}{\kappa_{\rm R,cz}}\right)^{-1}. \qquad \text{(A2)}$$

The following quantities are those at the base of the convection zone: $T_{\rm cz} = 2.3\times10^6$ K, $\rho_{\rm cz} = 0.21$ g cm^{-3}, $\kappa_{\rm R,cz} = 19$ cm^2 g^{-1}, $\ln\Lambda_{\rm cz} = 2.5$, $\nu_{\rm cz} = 27$ cm^2 s^{-1}, $\eta_{\rm cz} = 410$ cm^2 s^{-1} and $\kappa_{\rm cz} = 1.4\times10^7$ cm^2 s^{-1}.

APPENDIX B: MODEL EQUATIONS IN SPHERICAL COORDINATES

The model equations described in the system (9) are now expanded in a spherical coordinate system (r, θ, ϕ), with $\tilde{\boldsymbol{u}} = (\tilde{u}_r, \tilde{u}_\theta, \tilde{u}_\phi)$, $\boldsymbol{B} = (B_r, B_\theta, B_\phi)$ and $\boldsymbol{j} = (j_r, j_\theta, j_\phi)$. The r component of the momentum equation is

$$-\overline{\rho}\sin\theta\left(2\overline{\Omega} + \frac{\tilde{u}_\phi}{r\sin\theta}\right)\tilde{u}_\phi = -\frac{\partial\tilde{p}}{\partial r} - \tilde{\rho}\frac{{\rm d}\overline{\Phi}}{{\rm d}r} + j_\theta B_\phi - j_\phi B_\theta + f_\nu(\nabla\cdot\Pi)_r. \qquad \text{(B1)}$$

The θ component of the momentum equation is

$$-\overline{\rho}\cos\theta\left(2\overline{\Omega} + \frac{\tilde{u}_\phi}{r\sin\theta}\right)\tilde{u}_\phi = j_\phi B_r - j_r B_\theta + f_\nu(\nabla\cdot\Pi)_\theta. \qquad \text{(B2)}$$

The ϕ component of the momentum equation is

$$\overline{\rho}\left(2\overline{\Omega} + \frac{\tilde{u}_\phi}{r\sin\theta}\right)(\cos\theta\tilde{u}_\theta + \sin\theta\tilde{u}_r) = j_r B_\theta - j_\theta B_r + f_\nu(\nabla\cdot\Pi)_\phi, \qquad \text{(B3)}$$

where the role of f_ν was discussed in section 3.3.1. The divergence of the viscous stress tensor, for a stratified fluid, can be derived from Batchelor (1994 edition, p. 147 and 601). The mass conservation equation is

$$\frac{1}{r^2}\frac{\partial}{\partial r}\left(r^2\overline{\rho}\tilde{u}_r\right) + \frac{\overline{\rho}}{r\sin\theta}\frac{\partial}{\partial\theta}(\sin\theta\tilde{u}_\theta) = 0. \qquad \text{(B4)}$$

The thermal energy equation can be rewritten as (see SZ92)

$$\frac{\overline{\rho}c_{\rm p}\overline{T}N^2}{g}\tilde{u}_r = \frac{f_\kappa}{r^2}\frac{\partial}{\partial r}\left(r^2\overline{k}\frac{\partial\tilde{T}}{\partial r}\right) + \frac{f_\kappa\overline{k}}{r^2\sin\theta}\frac{\partial}{\partial\theta}\left(\sin\theta\frac{\partial\tilde{T}}{\partial\theta}\right), \qquad \text{(B5)}$$

where $g = {\rm d}\Phi/{\rm d}r$ and N is the Brunt–Vaisala (buoyancy) frequency.

The equation for the conservation of magnetic flux can be integrated once, and axial symmetry implies that

$$\tilde{u}_r B_\theta - \tilde{u}_\theta B_r = f_\eta\overline{\eta}\left[\frac{1}{r}\frac{\partial}{\partial r}(rB_\phi) - \frac{1}{r}\frac{\partial B_r}{\partial\theta}\right]. \qquad \text{(B6)}$$

The ϕ component of the equation of conservation of magnetic flux is

$$\frac{1}{r}\frac{\partial}{\partial r}(r\tilde{u}_\phi B_r - r\tilde{u}_r B_\phi) - \frac{1}{r}\frac{\partial}{\partial\theta}(\tilde{u}_\theta B_\phi - \tilde{u}_\phi B_\theta) = -\frac{f_\eta}{r}\frac{\partial}{\partial r}\left[\overline{\eta}\frac{\partial}{\partial r}(rB_\phi)\right] - \frac{f_\eta\overline{\eta}}{r^2}\frac{\partial}{\partial\theta}\left[\frac{1}{\sin\theta}\frac{\partial}{\partial\theta}(\sin\theta B_\phi)\right]. \qquad \text{(B7)}$$

Finally, the solenoidal condition is

$$\frac{1}{r^2}\frac{\partial}{\partial r}\left(r^2B_r\right) + \frac{1}{r\sin\theta}\frac{\partial}{\partial\theta}(\sin\theta B_\theta) = 0. \qquad \text{(B8)}$$

APPENDIX C: NUMERICAL IMPLEMENTATION OF THE EQUATIONS

Numerical implementation of the equations is done by defining the non-dimensional independent variables $x = r/{\rm R}_\odot$ and $\mu = \cos\theta$, and by working with the non-dimensional dependent variables

$$\hat{u} = \frac{\tilde{u}_r}{{\rm R}_\odot\Omega_{\rm eq}}, \hat{v} = \frac{\sin\theta\tilde{u}_\theta}{{\rm R}_\odot\Omega_{\rm eq}}, \hat{L} = \frac{r\sin\theta\tilde{u}_\phi}{{\rm R}_\odot^2\Omega_{\rm eq}},$$
$$\hat{B} = \frac{B_r}{B_0}, \hat{b} = \frac{\sin\theta B_\theta}{B_0}, \hat{S} = \frac{r\sin\theta B_\phi}{{\rm R}_\odot B_0}, \hat{J} = \frac{4\pi r\sin\theta j_\phi}{B_0}. \qquad \text{(C1)}$$

The perturbed thermodynamical quantities are also normalized with

$$\hat{\rho} = \frac{\tilde{\rho}}{\rho_0}, \hat{T} = \frac{\tilde{T}}{T_0}, \hat{p} = \frac{\tilde{p}}{p_0}, \qquad \text{(C2)}$$

where $\rho_0 = 1$ g cm^{-3}, $T_0 = 1$ K, and $p_0 = \rho_0{\rm R}_\odot^2\overline{\Omega}^2$.

The symmetries of the system in the latitudial coordinate θ suggest the expansion of the dependent variables on to Fourier modes, which are equivalent to Chebishev polynomials of the variable μ since the nth-order Chebishev polynomial T_n is defined as

$$T_n(\mu) = \cos(n\theta). \qquad \text{(C3)}$$

We assume symmetry across the equator for the radial velocity, the angular velocity, the thermodynamical quantities and the latitudinal

component of the magnetic field. Antisymmetry across the equator is then required for consistency for the latitudinal velocity as well as the radial and toroidal components of the magnetic field. In addition, we require that the total mass flux across a spherical surface be null. This leads to the suggested expansion:

$$\begin{aligned}
\hat{u}(x,\mu) &= \sum_{n=1}^{N} \psi_n(x) \frac{\partial}{\partial \mu}\left[(1-\mu^2) T_{2n-1}(\mu)\right], \\
\hat{v}(x,\mu) &= (1-\mu^2) \sum_{n=1}^{N} v_n(x) T_{2n-1}(\mu), \\
\hat{L}(x,\mu) &= (1-\mu^2) \sum_{n=1}^{N} L_n(x) T_{2n-2}(\mu), \\
\hat{p}(x,\mu) &= \sum_{n=1}^{N} p_n(x) T_{2n-2}(\mu), \\
\hat{\rho}(x,\mu) &= \sum_{n=1}^{N} \rho_n(x) T_{2n-2}(\mu), \\
\hat{T}(x,\mu) &= \sum_{n=1}^{N} \Theta_n(x) T_{2n-2}(\mu), \\
\hat{B}(x,\mu) &= \sum_{n=1}^{N} B_n(x) T_{2n-1}(\mu), \\
\hat{b}(x,\mu) &= (1-\mu^2) \sum_{n=1}^{N} b_n(x) T_{2n-2}(\mu), \\
\hat{S}(x,\mu) &= (1-\mu^2) \sum_{n=1}^{N} S_n(x) T_{2n-1}(\mu), \\
\hat{J}(x,\mu) &= (1-\mu^2) \sum_{n=1}^{N} J_n(x) T_{2n-1}(\mu),
\end{aligned} \tag{C4}$$

where each sum is truncated to retain the first N modes only. The equations are expanded using the ansatz (C4), then projected back on to the first N Chebishev modes (of relevant parity). The quadratic terms are simplified analytically using the standard formulae $2T_n(\mu)\ T_{\rm m}(\mu) = [T_{n+m}(\mu) + T_{n-m}(\mu)]$ and $T_n(\mu) = T_{-n}(\mu)$, as well as a variety of others that have been summarized by Garaud (2001, p. 200). This procedure yields a combination of $12N$ first-order ODEs and $3N$ algebraic equations for a total of $15N$ dependent variables, namely $\{\psi_n\}$, $\{v_n\}$, $\{L_n\}$, $\{T_n\}$ and $\{S_n\}$ (and their respective radial first derivatives), as well as $\{p_n\}$, $\{\rho_n\}$, $\{B_n\}$, $\{b_n\}$ and $\{J_n\}$ for $n = 1, \ldots, N$.

These equations are solved using a versatile variant of the standard NRK relaxation solver (see e.g. Press et al. 1996, chapter 17.3) developed by Garaud (2001, p. 108). The added feature compared with the standard algorithm permits the solution of any set of equations that can be written in the form

$$\sum_{j=1}^{N_{\rm v}} M_{ij}(\boldsymbol{y}, x) \frac{\partial y_j}{\partial x} = f_i(\boldsymbol{y}, x) \quad \text{for } i = 1, \ldots, N_{\rm v}, \tag{C5}$$

where x is the independent variable, $\boldsymbol{y} = \{y_i\}$ is the vector containing the $N_{\rm v}$ dependent variables, and $M_{ij}(\boldsymbol{y}, x)$ and $f_i(\boldsymbol{y}, x)$ can be any non-linear function of x and $\boldsymbol{y}$. One of the many advantages of this form is that algebraic equations are straightforwardly treated as any other equation by setting $M_{ij} = 0$ for all j and for i corresponding to the relevant equation(s).

As in the standard relaxation algorithm (see Press et al. 1996) most of the computational cost (both in terms of time and memory) arises from reading and inverting a block-tridiagonal matrix containing $N_x + 1$ rows of three blocks[9] (where N_x is equal to the number of meshpoints used, typically between 2000 and 3000), and where each block has size[10] $N_{\rm v} \times N_{\rm v}$ where $N_{\rm v}$ is the total number of dependent variables ($N_{\rm v} = 15N$, where N is 60–80 for a typical run). Calculation of the matrix components, followed by its inversion using serial partial pivoting can require several hours per iteration on a high-end desktop. In addition, memory becomes an issue since the standard algorithm typically requires the storage of N_x double-precision arrays of size $N_{\rm v} \times N_{\rm v}/2$ before back-substitution can proceed. For this reason, we have developed a parallel version of the NRK solver.

APPENDIX D: PARALLEL NRK ALGORITHM

A serial, simple and efficient way of inverting the typical block-tridiagonal linear systems arising from two-point boundary value problems is described by Press et al. (1996). Given the matrix structure

$$\begin{bmatrix}
M & R & & & & & & & \\
L & M & R & & & & & & \\
 & L & M & R & & & & & \\
 & & L & M & R & & & & \\
 & & & L & M & R & & & \\
 & & & & L & M & R & & \\
 & & & & & L & M & R & \\
 & & & & & & L & M & R \\
 & & & & & & & L & M
\end{bmatrix} \tag{D1}$$

the algorithm consists in diagonalizing the first top M (middle) block using Gauss–Jordan elimination with partial implicit pivoting, and storing the resulting modified R block and right-hand side for later back-substitution. Moving on to the second block-row, we zero the L block, diagonalize the M block and store the modified R block (and modified right-hand side vector), and so forth. The resulting matrix structure is

$$\begin{bmatrix}
I & S & & & & & & & \\
0 & I & S & & & & & & \\
 & 0 & I & S & & & & & \\
 & & 0 & I & S & & & & \\
 & & & 0 & I & S & & & \\
 & & & & 0 & I & S & & \\
 & & & & & 0 & I & S & \\
 & & & & & & 0 & I & S \\
 & & & & & & & 0 & I
\end{bmatrix} \tag{D2}$$

where 0 denotes a 'zeroed' block, I is the identity, and S is a stored block. The last step involves sweeping the matrix back from bottom to top to back-substitute for the unknown variables. This method requires minimal storage: first, each block-row only needs to be read just before being processed and secondly, the back-substitution step only requires knowledge of the blocks S and modified right-hand side vector.

Inverting the same linear system in parallel is not obvious since the previous algorithm is inherently serial. A standard parallel method used for block tridiagonal matrices is cyclic reduction (see

[9] Except for the boundary blocks, of course.
[10] Again, except for the boundary blocks, which are smaller.

Golub & Ortega 1993). In this case, the number of variables is successively halved by repeating the following reduction algorithm: diagonalize all M blocks in odd block-rows by partial implicit pivoting, then zero the R and L matrices directly above and below by Gaussian elimination. The resulting matrix after the first reduction is

$$\begin{bmatrix}
I & S & & & & & & & \\
0 & X & 0 & X & & & & & \\
 & S & I & S & & & & & \\
 & X & 0 & X & 0 & X & & & \\
 & & & S & I & S & & & \\
 & & & X & 0 & X & 0 & X & \\
 & & & & & S & I & S & \\
 & & & & & X & 0 & X & 0 \\
 & & & & & & & S & I
\end{bmatrix} \tag{D3}$$

where S denotes a block that has been modified and needs to be stored for later back-substitution, and X denotes blocks that have been modified and will be used in the next reduction step. Note that all of the remaining X blocks (in the odd block-rows) form a new block-tridiagonal system for roughly half the number of variables (more precisely, if the initial number of block-rows is $2^k - 1$ then the reduction step reduces it to $2^{k-1} - 1$). The algorithm can be repeated until only one block is left and finally inverted, at which point back-substitution can begin. The main advantage of the method is its inherently parallelizable nature, since each process can be instructed to reduce a number of blocks more or less independently of the others; communication between processes is minimal until the final steps where the number of remaining block-rows is equal to the number of processes. Unfortunately, the stability of this cyclic reduction algorithm is much weaker that the stability of the serial algorithm (since the matrix cannot be globally pivoted), and was found to be unreliable for our purpose.

An alternative parallel algorithm was constructed, loosely based on the work of Wright (1992). The block-rows are first equally distributed between the processes. A first sweeping reduction akin to the serial algorithm is performed starting from the top block-row down to the second-to-last block-row in each process[11] to transform the matrix to

$$\left[\begin{array}{cccccccccc}
I & S & & & & & & & & \\
0 & I & S & & & & & & & \\
 & 0 & I & S & & & & & & \\
 & & 0 & X & X & & & & & \\
\hline
 & & & S & I & S & & & & \\
 & & & S & 0 & I & S & & & \\
 & & & S & & 0 & I & S & & \\
 & & & X & & & 0 & X & X & \\
\hline
 & & & & & & & S & I & S \\
 & & & & & & & S & 0 & I \\
 & & & & & & & S & & 0 \\
 & & & & & & & X & & \\
 & & & & & & & & 0 & I
\end{array}\right] \tag{D4}$$

[11] Except in the last process, which is swept all the way.

(assuming in the case shown here that 12 block-rows are equally distributed between three processes). Again, by convention all S blocks denote blocks that need to be stored for back-substitution, while X blocks are blocks that will be further modified. Until this point, work in each process can be done without communication with other processes.

At the end of the sweeping step, each process sends its very last block-row to the following process. Thus the blocks are redistributed as

$$\left[\begin{array}{cccccccccc}
I & S & & & & & & & & \\
0 & I & S & & & & & & & \\
 & 0 & I & S & & & & & & \\
\hline
 & & 0 & X & X & & & & & \\
 & & & S & I & S & & & & \\
 & & & S & 0 & I & S & & & \\
 & & & S & & 0 & I & S & & \\
\hline
 & & & X & & & 0 & X & X & \\
 & & & & & & & S & I & S \\
 & & & & & & & S & 0 & I \\
 & & & & & & & S & & 0 \\
 & & & & & & & X & & \\
 & & & & & & & & 0 & I
\end{array}\right] \tag{D5}$$

Each process can then continue eliminating undesirable variables from its top block-row by Gaussian elimination with the successive block-rows below, until the following form is achieved:

$$\left[\begin{array}{cccccccccc}
I & S & & & & & & & & \\
0 & I & S & & & & & & & \\
 & 0 & I & S & & & & & & \\
\hline
 & & 0 & X & 0 & 0 & 0 & X & & \\
 & & & S & I & S & & & & \\
 & & & S & 0 & I & S & & & \\
 & & & S & & 0 & I & S & & \\
\hline
 & & & X & & & 0 & X & 0 & 0 & 0 & X \\
 & & & & & & & S & I & S & & \\
 & & & & & & & S & 0 & I & S & \\
 & & & & & & & S & & 0 & I & S \\
 & & & & & & & X & & & 0 & I
\end{array}\right] \tag{D6}$$

At this point, the top rows in each process can be combined into a much-reduced block tridiagonal system. Solution from here on proceeds with a cyclic reduction of the remaining blocks across processes, followed by a back-substitution step.

The operation count of this algorithm is the same as that of the standard cyclic reduction. The advantages of this algorithm over the standard cyclic reduction are twofold. First, it is found to be much more stable (Wright 1992). Secondly, it is far more versatile, since the standard algorithm only performs ideally with a number of block-rows equal to $2^k + 1$ (for any integer k), which seriously constrains the number of meshpoints one is allowed to select. On

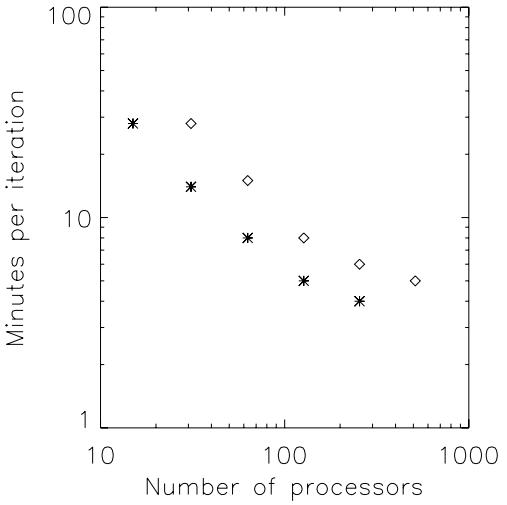

Figure D1. Scaling properties of the parallel NRK algorithm RELAX for the simulations presented in this paper. The stars correspond to a simulation with 60 modes (i.e. 900 equations) and 1000 meshpoints. The diamonds correspond to the same simulation but with 2000 meshpoints.

the other hand, in this algorithm it is always possible to balance the load (for any number of meshpoints) in such a way that any process contains at most one more block-row than the average.

The scalability of the algorithm is naturally excellent until the number of processes approaches a tenth of the number of meshpoints. This is illustrated in Fig. D1.

Finally, we note that the user interface of the complete associated parallel version of the NRK algorithm (RELAX) is entirely identical to that of the widely used serial NRK algorithm written by Gough & Moore. Transfer between the parallel and serial version should be transparent to the user. The RELAX algorithm is freely available upon request from P. Garaud.

This paper has been typeset from a TEX/LATEX file prepared by the author.